

Constraint on Matter Power Spectrum on $10^6 - 10^9 M_\odot$ Scales from τ_e

Renyue Cen¹

ABSTRACT

An analysis of the physics-rich endgame of reionization at $z = 5.7$ is performed, utilizing jointly the observations of the Ly α forest, the mean free path of ionizing photons, the luminosity function of galaxies and new physical insight. We find that an upper limit on τ_e provides a constraint on the minimum mean free path (of ionizing photons) that is primarily due to dwarf galaxies, which in turn yields a new and yet the strongest constraint on the matter power spectrum on $10^6 - 10^9 M_\odot$ scales. With the latest Planck measurements of $\tau_e = 0.055 \pm 0.009$, we can place an upper limit of $(8.9 \times 10^6, 3.8 \times 10^7, 4.2 \times 10^8) M_\odot$ on the lower cutoff mass of the halo mass function, or equivalent a lower limit on warm dark matter particle mass $m_x \geq (15.1, 9.8, 4.6)\text{keV}$ or on sterile neutrino mass $m_s \geq (161, 90, 33)\text{keV}$, at $(1, 1.4, 2.2)\sigma$ confidence level, respectively.

1. Introduction

The Gunn & Peterson (1965) optical depth of Ly α photons provides the strongest and most sensitive constraint on the neutral hydrogen fraction of the intergalactic medium (IGM). The integrated electron scattering optical depth of the universe provides a complementary constraint on the ionized fraction of the IGM, but is insensitive to the neutral hydrogen fraction as long as the IGM is mostly ionized.

Recent measurements of the electron scattering optical depths of the IGM by the cosmic microwave background radiation experiments (e.g., Hinshaw et al. 2013; Planck Collaboration et al. 2015) suggest that it may be significantly below redshift $z = 12$ before the universe becomes half reionized. The observations of the high redshift ($z > 6$) quasar absorption spectra from the Sloan Digital Sky Survey (SDSS) and others (e.g., Fan et al. 2006) and arguments based on the slowly and continuously evolving IGM opacity (e.g., Becker et al. 2007) suggest that only at $z = 5.7$ the universe is sufficiently ionized to allow for detectable transmission of Ly α photons hence definitive measurements of (low enough) Ly α (and higher order Lyman series) optical depth.

It is generally accepted that stars are primarily responsible for producing most of the ionizing photons for cosmological reionization. While it seems relatively secure to further suggest that the reionization process has begun at $z \geq 10$ based on analysis of expected emergence of first galaxies in the standard cold dark matter model (e.g., Trac et al. 2015), the combination of these independent observational indications now paints a reionization picture that is rapidly

evolving at $z = 6 - 10$. Two important implications are that the so-called first galaxies that form out of primordial gas may be closer to us than thought before and that Population III (Pop III) stars formed with metal-free gas may extend to more accessible redshifts.

In this contribution we perform a detailed analysis of the endgame of the cosmological reionization at $z = 5.7$. We examine joint constraints on the IGM from considerations of both global and local ionization balances observationally and, for the first time, self-consistently in the context of the standard cold dark matter model. We find reasonable concordance between $\text{Ly}\alpha$ optical depth, Lyman continuum (LyC) mean free path (mfp) λ_{mfp} and global recombination rate of hydrogen observationally and theoretically. We solve the global reionization equation, given the emissivity evolution in the context of the standard cold dark matter model normalized to the boundary conditions of required emissivity at $z = 5.7$ and reionization completing at $z = 5.7$. We provide a detailed analysis of the attainable solutions of reionization histories to shed light on the overall topological evolution of the HII regions, the evolution of the $\text{Ly}\alpha$ emitters, the neutral fraction of the IGM, and a new and powerful constraint on the matter power spectrum on small scales hence dark matter particle properties.

Our focus here is on placing a yet the strongest constraint on the scale-scale power in the cosmological model and, specifically, the strongest lower bound on the mass of warm dark matter particles. The physical insight on this particular point is new and may be described briefly as follows. The state of the IGM at $z = 5.7$ is well fixed by the Gunn & Peterson (1965) optical depth of $\text{Ly}\alpha$ photons, which in turn provides a tight constraint on the photoionization rate Γ at $z = 5.7$ in the post-reionization epoch. Since Γ at $z = 5.7$ is equal to $\dot{N}_{\text{ion,IGM}}\lambda_{\text{mfp}}\bar{\sigma}_{\text{ion}}$, where $\dot{N}_{\text{ion,IGM}}$ is the global mean of effective ionization photon emissivity at $z = 5.7$, λ_{mfp} is the mean free path of ionizing photons at $z = 5.7$ and $\bar{\sigma}_{\text{ion}}$ is the spectrum-weighted mean photoionization cross section, a constant. Thus, a tight constraint on Γ at $z = 5.7$ is equivalent to an equally tight constraint on the product $\dot{N}_{\text{ion,IGM}}\lambda_{\text{mfp}}$ at $z = 5.7$. Note that $\dot{N}_{\text{ion,IGM}}$ already takes into account the escape fraction of ionizing photon from ionization sources (e.g., galaxies and others). The degeneracy between $\dot{N}_{\text{ion,IGM}}$ and λ_{mfp} can be broken, if one considers, jointly, a separate constraint placed by an upper limit on the integrated electron scattering optical depth of the universe τ_e from the latest cosmic microwave background radiation experiments (e.g., Planck Collaboration et al. 2016). This is where our new physical insight comes in. We point out that, when the product $\dot{N}_{\text{ion,IGM}}\lambda_{\text{mfp}}$ is fixed, a higher λ_{mfp} would require a lower $\dot{N}_{\text{ion,IGM}}$, which in turn would cause the reionization process to shift to lower redshift hence give rise to a lower τ_e . In other words, there is a negative correlation between λ_{mfp} and τ_e . Since more small-scale power results in a lower λ_{mfp} , there is then a negative correlation between the amount of small-scale power and τ_e - more small-scale power leads to lower τ_e . As a result, an upper bound on τ_e placed by the latest CMB observations would translate to a lower bound on the amount of small-scale power hence a lower bound on the particle mass in the context of the warm dark matter model. This is the scientific focus of this paper.

2. On Sinks and Sources of Lyman Continuum at $z = 5.7$

2.1. Global Balance of Emission and Recombination

The hydrogen recombination rate per unit comoving volume at redshift z is

$$\dot{N}_{\text{rec}} = C_{\text{HII}}\alpha_{\text{B}}(\text{T})[1 + Y_{\text{p}}/4(1 - Y_{\text{p}})]n_{\text{H},0}^2(1 + z)^3 \quad (1)$$

and the corresponding helium I recombination rate is

$$\dot{N}_{\text{HeI,rec}} = C_{\text{HII}}\alpha_{\text{B}}(\text{HeI}, \text{T})[1 + Y_{\text{p}}/4(1 - Y_{\text{p}})][Y_{\text{p}}/4(1 - Y_{\text{p}})]n_{\text{H},0}^2(1 + z)^3, \quad (2)$$

where $n_{\text{H},0} = 2.0 \times 10^{-7}(\Omega_{\text{B}}/0.048)\text{cm}^{-3}$ is the mean hydrogen number density at $z = 0$, $Y_{\text{p}} = 0.24$ the primordial helium mass fraction, C_{HII} is the clumping factor of the recombining medium. The case B recombination coefficient

$\alpha_{\text{B}}(\text{T}) = (2.59, 2.52) \times 10^{-13} \text{ cm}^3\text{s}^{-1}$ at $\text{T} = (10^4, 2 \times 10^4)\text{K}$ (Osterbrock 1989). The case B He I recombination coefficient is $\alpha_{\text{B}}(\text{HeI}, \text{T}) = (2.73, 1.55) \times 10^{-13} \text{ cm}^3 \text{ s}^{-1}$ at $\text{T} = (10^4, 2 \times 10^4)\text{K}$ (Osterbrock 1989).

To prevent the already ionized IGM from recombining, the amount of ionizing photons entering the IGM has to be, at least, equal to the total recombination rate, resulting in the well known minimum requirement of ionizing photon production rate (e.g., Madau et al. 1999)

$$\begin{aligned} \dot{N}_{\text{ion,global}} &\geq \dot{N}_{\text{rec}} + \dot{N}_{\text{HeI,rec}} \\ &= 3.4 \times 10^{50} (C_{\text{HII}}/3.2)(\Omega_{\text{b}}/0.048)^2((1+z)/6.7)^3 \text{cMpc}^{-3}\text{s}^{-1} \text{ for } \text{T} = 10^4\text{K} \\ &= 3.2 \times 10^{50} (C_{\text{HII}}/3.2)(\Omega_{\text{b}}/0.048)^2((1+z)/6.7)^3 \text{cMpc}^{-3}\text{s}^{-1} \text{ for } \text{T} = 2 \times 10^4\text{K}, \end{aligned} \quad (3)$$

assuming that helium II is not ionized. We shall call this constraint expressed in Eq 3 “global constraint”. For clarity we will adopt the convention to use cMpc and pMpc to denote comoving and proper Mpc, respectively. Early hydrodynamical simulations suggest $C_{\text{HII}} \sim 10 - 40$ at $z < 8$ (e.g., Gnedin & Ostriker 1997). More recent simulations that separate out dense interstellar medium (ISM) from the IGM indicate a lower $C_{\text{HII}} \sim 1 - 6$ at $z \sim 6$ (e.g., Sokasian et al. 2003; Iliev et al. 2006; Pawlik et al. 2009; Shull et al. 2012; Finlator et al. 2012). Pawlik et al. (2009) give

$$\begin{aligned} C_{\text{HII}} &= 3.2 \quad \text{for } z \leq 10 \\ &= 1 + \exp(-0.28z + 3.59) \quad \text{for } z > 10, \end{aligned} \quad (4)$$

which we will use in the calculations below. As we demonstrate later, the value $C_{\text{HII}} = 3.2$ at $z = 5.7$ is concordant between considerations of global and local ionization balances.

2.2. Local Balance of Ionization and Recombination

A second, independent determination of ionizing photon production rate can be obtained from the $\text{Ly}\alpha$ optical depth around cosmic mean density, $\tau_{\text{Ly}\alpha}$, i.e., the Gunn & Peterson (1965)

optical depth, at $z = 5.7$, where observational measurements are available. Because of the large cross section of neutral hydrogen for Ly α scattering, $\tau_{\text{Ly}\alpha}$ is the most sensitive probe of neutral medium in the low neutral-fraction regime. From the SDSS observations of high redshift quasar absorption spectra $\tau_{\text{Ly}\alpha}$ is directly measured (Fan et al. 2002; Fan et al. 2006). When analyzed in conjunction with density distributions of the IGM from hydrodynamic simulations, one can infer both the volume weighted neutral fraction and the ionization rate Γ , expressed in units of 10^{-12}s^{-1} , Γ_{-12} . Because the mean density regions that determine the volume-weighted neutral fraction are well resolved in simulations (i.e., the simulation resolution is much finer than the Jeans scale of the photoionized IGM), the uncertainty on the determined volume-weighted neutral fraction is small and does not depend sensitively on cosmological parameters, either. The analysis performed by Cen & McDonald (2002) uses a smaller sample of SDSS quasars coupled with simulations of Cen et al. (1994). The analysis performed by Fan et al. (2006) utilizes a larger quasars sample and the density distribution function of Miralda-Escudé et al. (2000). Both studies derive, independently, $\Gamma_{-12} \sim 0.20$. For the subsequent calculations, we will use

$$\Gamma_{-12} = 0.20_{-0.06}^{+0.11} \quad (5)$$

at $z = 5.7$ from Fan et al. (2006).

Under the assumption that the spatial scales of fluctuations (or clustering scales) for both sources and sinks are substantially smaller than the mean free path λ_{mfp} of LyC photons, then the (approximately uniform) ionizing flux at any spatial point is

$$F_{\text{ion}} = \int_0^\infty \frac{\dot{N}_{\text{ion,IGM}}}{4\pi r^2} \exp(-r/\lambda_{\text{mfp}}) 4\pi r^2 dr = \dot{N}_{\text{ion,IGM}} \lambda_{\text{mfp}}, \quad (6)$$

where $\dot{N}_{\text{ion,IGM}}$ is the mean emissivity of ionizing photons entering the IGM. We note that the 2-point correlation length of galaxies at $z = 5.7$ is 4 – 5cMpc (e.g., Ouchi et al. 2010), much smaller than $\lambda_{\text{mfp}} \sim 30 - 60\text{cMpc}$, which we will discuss later. Therefore, the above assumption is a good one, so long as stellar sources are the main driver of cosmological reionization. We expect that radiation flux fluctuations would be on the order of the ratio of the two lengths scales above, i.e., $\sim 10\%$. As we will show later that, in the context of the ΛCDM model, λ_{mfp} depends on Γ approximately as $\lambda_{\text{mfp}} \propto \Gamma^{-0.28}$. Thus, we expect that the uniform radiation assumption is accurate statistically for computing the mean λ_{mfp} at 1 – 3% level, with negligible systematic biases. The hydrogen ionization rate

$$\Gamma = F_{\text{ion}} \bar{\sigma}_{\text{ion}} = \dot{N}_{\text{ion,IGM}} \lambda_{\text{mfp}} \bar{\sigma}_{\text{ion}}, \quad (7)$$

where $\bar{\sigma}_{\text{ion}}$ is the spectrum-weighted mean photoionization cross section,

$$\bar{\sigma}_{\text{ion}} \equiv \frac{\int_{13.6\text{eV}}^\infty \frac{f_\nu}{h\nu} \sigma_{\text{H}}(\nu) d\nu}{\int_{13.6\text{eV}}^\infty \frac{f_\nu}{h\nu} d\nu}, \quad (8)$$

where $\sigma_{\text{H}}(\nu)$ is the photon energy-dependent hydrogen ionization cross section, f_ν is the ionizing photon spectrum. We will use f_ν for Pop II stars of metallicity $Z = 0.05 Z_\odot$ from Tumlinson

et al. (2001), which may be approximated as

$$\begin{aligned} f_\nu &\propto \nu^0 && \text{for } \nu = 13.6 - 24.6\text{eV} \\ &\propto \nu^{-1} && \text{for } \nu = 24.6 - 46\text{eV} \\ &\propto \nu^{-\infty} && \text{for } \nu > 46\text{eV}, \end{aligned}$$

which results in the fiducial value that we will use in our calculations at $z = 5.7$,

$$\bar{\sigma}_{\text{ion}} = 3.16 \times 10^{-18} \text{ cm}^2. \quad (9)$$

Combining Eq (5, 7, 9) gives the constraint on comoving emissivity at $z = 5.7$ from Gunn-Peterson optical depth, named "local constraint",

$$\dot{N}_{\text{ion,local}} = 2.7 \times 10^{50} \left(\frac{\Gamma_{-12}}{0.2} \right) \left(\frac{\bar{\sigma}_{\text{ion}}}{3.16 \times 10^{-18} \text{ cm}^2} \right)^{-1} \left(\frac{\lambda_{\text{mfp}}}{7.6 \text{ pMpc}} \right)^{-1} \text{ cMpc}^{-3} \text{ s}^{-1}. \quad (10)$$

In Eq 10 it is seen that there is a significant, linearly inverse dependence of $\dot{N}_{\text{ion,local}}$ on λ_{mfp} , which we now discuss in length observationally here and theoretically in the next subsection.

Traditionally, λ_{mfp} is determined by counting the incidence frequency of Lyman limit systems (LLSs) (e.g., Storrie-Lombardi et al. 1994; Stengler-Larrea et al. 1995; Songaila & Cowie 2010; Ribaldo et al. 2011; O'Meara et al. 2013) and generally found to be in the range of $\lambda_{\text{mfp}} = 5 - 10 \text{ pMpc}$ at $z = 5.7$, when extrapolated from lower redshift trends. This method to determine λ_{mfp} contains some ambiguity as to the dependence of the incidence frequency on exact choice of column density threshold of LLSs, and uncertainties related to absorption system identifications (such as line blending) and collective absorption due to clustering of absorbers. A more direct approach to determining λ_{mfp} is to measure the optical depth at Lyman limit directly, as pioneered by Prochaska et al. (2009). A recent application of that technique to a large sample of (163) high redshift quasars is cast into fitting formula $\lambda_{\text{mfp}} = 37[(1+z)/5]^{-5.4 \pm 0.4} \text{ pMpc}$ that covers up to redshift $z = 5.5$ (Worseck et al. 2014). Extrapolating this formula to $z = 5.7$ results in a median value of 7.6 pMpc,

$$\lambda_{\text{mfp}} = 7.6_{-0.8}^{+1.0} \text{ pMpc}, \quad (11)$$

with the 1 and 2σ range of 6.8 – 8.6 pMpc and 6.0 – 9.6 pMpc, respectively. It is seen that the directly measured λ_{mfp} are in broad agreement with those based on counting LLSs, which is reassuring. Nevertheless, it is prudent to bear in mind a significant caveat that λ_{mfp} at $z = 5.7$ is not directly observed but requires extrapolation from lower redshift data.

2.3. Concordance of Independent Observations at $z = 5.7$

We now combine three independent sets of observational constraints on \dot{N}_{ion} , Γ and λ_{mfp} on the $\Gamma - \lambda_{\text{mfp}}$ plane, shown in Figure 1: (1) the observed λ_{mfp} from Worseck et al. (2014)

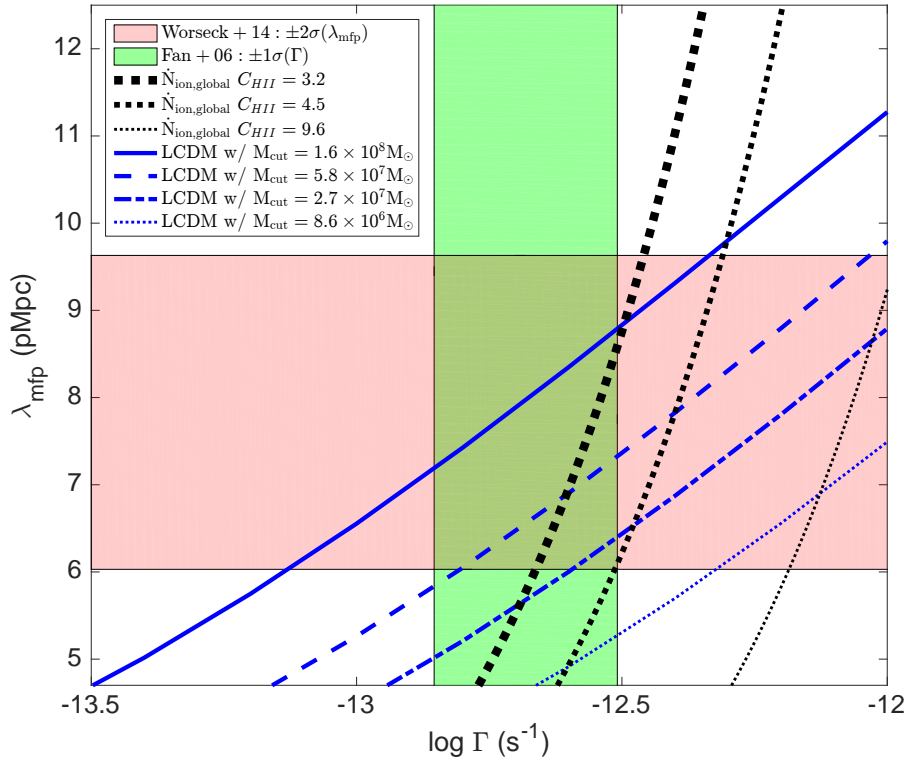


Fig. 1.— shows four independent sets of constraints on the $\Gamma - \lambda_{\text{mfp}}$ plane: (1) the observed λ_{mfp} from Worseck et al. (2014) based on LyC optical depth observed at $z < 5.5$ extrapolate to $z = 5.7$ (see Eq 11) shown as the red solid curve (mean), thick red dashed curves (1σ) and thin red dashed curves (2σ); (2) the observationally inferred 1σ range of Γ based on measurement of Ly α absorption optical depth at $z = 5.7$ from Fan et al. (2006) shown as the two vertical green dashed lines (see Eq 5); (3) lower bound based on a global balance between emissivity and recombination with Eq 3 assuming clumping factor $C_{\text{HII}} = (3.2, 4.5, 9.6)$ and gas temperature $T = 10^4$ K, shown as dotted black (thick, median thick, thin) curves; (4) the self-consistently calculated relation between Γ and λ_{mfp} in the standard Λ CDM model with a lower halo mass cutoff of $(1.6 \times 10^8, 5.8 \times 10^7, 2.7 \times 10^7, 8.6 \times 10^6) M_{\odot}$, respectively, corresponding to a virial temperature cutoff of $T_{\text{v,cutoff}} = (10^4, 5 \times 10^3, 3 \times 10^3, 1.4 \times 10^3)$ K.

based on Lyman continuum radiation optical depth at $z = 5.7$ (see Eq 11) are shown as the red solid curve (mean), thick red dashed curves (1σ) and thin red dashed curves (2σ); (2) the observationally inferred 1σ range of Γ based on measurement of Ly α absorption optical depth at $z = 5.7$ from Fan et al. (2006) are shown as the two vertical green dashed lines (see Eq 5); (3) lower bound based on a global balance between emissivity and recombination with Eq 3 assuming clumping factor $C_{\text{HII}} = (3.2, 4.5, 9.6)$ and gas temperature $T = 10^4$ K, shown as dotted black (thick, median thick, thin) curves.

To be conservative, we will use the 2σ range of λ_{mfp} from Worseck et al. (2014) for our

discussion, because of the possible additional, systematic uncertainty of using an extrapolated value from the observed highest redshift of $z = 5.5$ to $z = 5.7$. Thus, the allowed parameter space is enclosed by the two thin dashed red horizontal lines and the two vertical dashed green lines. This space is then further constrained by the requirement that only to the right of each of the dotted black curves is attainable, depending on the assumed clumping factor C_{HII} . The placement of this additional requirement on the plane suggests that $C_{\text{HII}} > 5$ at $z = 5.7$ may not be feasible but the values in Eq 4 that is obtained from recent radiation hydrodynamic simulations and adopted here are fully consistent with this constraint.

It is by no means guaranteed a priori that there is any parameter space left when all these three independent observational constraints are considered, due to uncertainties in individual observations. Hence, the fact that there is suggests a concordance among the independent observations.

2.4. Global Stellar Emissivity of Ionizing Photons at $z = 5.7$

Figure 1 in §2.4 summarizes the current state of constraints on the required emissivity of ionizing photons in the IGM at $z = 5.7$, in order to (1) keep the IGM ionized globally, (2) keep the IGM ionized locally as demanded by the optical depths probed by the hydrogen Lyman series absorption lines. The multi-faceted agreement is indeed quite remarkable, providing a validation of the different observations at $z = 5.7$ (in some cases extrapolation is needed) in the post-overlap epoch.

We now address “sources” of ionizing photons, in a fully self-consistent fashion, in the standard cold dark matter model. We follow the approach taken by Trac et al. (2015), to which the reader is referred for a more detailed description. Briefly, the method uses direct observations of galaxy luminosity functions at high redshift in the Hubble UDF to calibrate the star formation parameters in the model based on halo mass accretion rate functions in the Λ CDM model. Figure 2 shows a comparison of rest-frame FUV luminosity functions between the model based on the most recent cosmological parameters and observations at various redshifts. The observed LFs are most reliable at $z \leq 6$ and become less so towards higher redshifts, and perhaps less than trustworthy beyond $z = 8$ due to lack of spectroscopic confirmation at present. For a given small region/area, such as the UDF, cosmic variance becomes more problematic towards higher redshift. Additionally, it is possible that the observed LFs at high redshifts, in the midst of reionization, may be masked by possible reionization effects; this issue is significantly more acute for $\text{Ly}\alpha$ emitting galaxies (e.g., Mesinger et al. 2004; Haiman & Cen 2005; Dijkstra et al. 2007). These problems can be circumvented, if we normalize the model at $z = 6$ and use the “global” LFs from the model at high redshifts where direct observations lack or are unreliable. We take this approach.

From Figure 2 we see that the model LFs match observations well at $z = 6, 7$. The agreement is still good at $z = 8$, albeit with “noisier” observational data. There is very little to

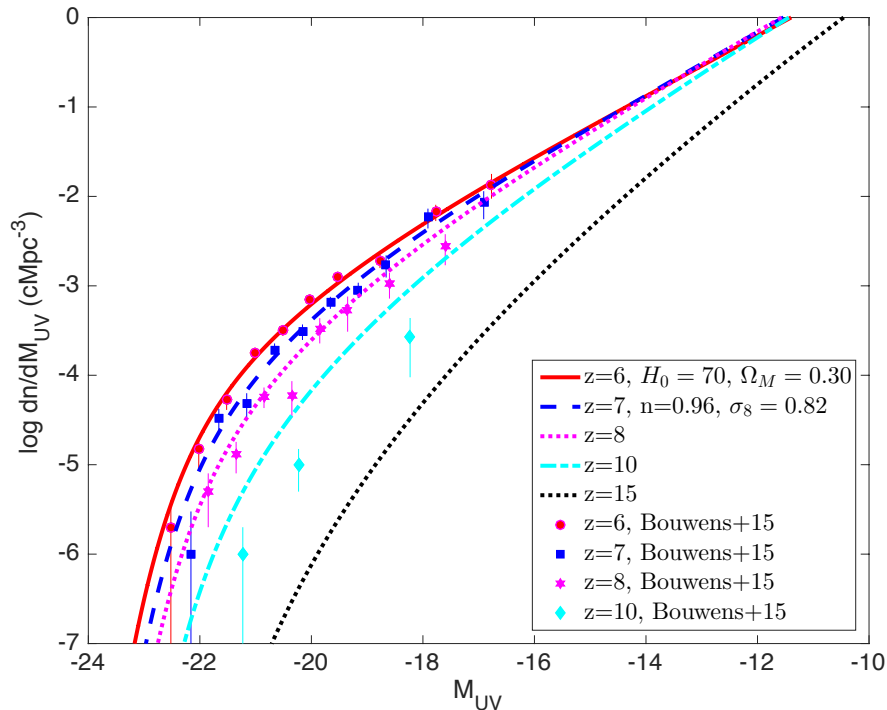


Fig. 2.— shows the galaxy luminosity functions predicted by the Λ CDM model at $z = 6$ (red solid curve), 7 (blue dashed curve), 8 (magenta dotted curve), 10 (cyan dot-dashed curve) and 15 (black dotted curve), which are compared to the observations at the four corresponding redshifts, shown as various symbols with corresponding colors. The observational data are from Bouwens et al. (2015).

glean from the comparison at $z = 10$, simply because the observational data lack both quantity and quality. Integrating the Schechter fits of the Bouwens et al. (2015) LF at $z = 6$ yields the intrinsic ionizing photon production rate from galaxies of

$$\begin{aligned}
 \dot{N}_{\text{ion,int}} &= 10^{51.52} \text{cMpc}^{-3} \text{s}^{-1} & \text{for } M_{\text{UV,limit}} = -12 \\
 &= 10^{51.57} \text{cMpc}^{-3} \text{s}^{-1} & \text{for } M_{\text{UV,limit}} = -10 \\
 &= 10^{51.61} \text{cMpc}^{-3} \text{s}^{-1} & \text{for } M_{\text{UV,limit}} = -8.
 \end{aligned} \tag{12}$$

In obtaining $\dot{N}_{\text{ion,int}}$, we have used a relation between ionizing photo production rate per unit FUV spectral density from (Robertson et al. 2013),

$$\xi_{\text{ion}} \equiv \frac{\dot{N}_{\text{ion}}/\text{cMpc}^{-3} \text{s}^{-1}}{L_{\text{UV}}/\text{erg s}^{-1} \text{Hz}^{-1} \text{cMpc}^{-3}} = 10^{25.2}, \tag{13}$$

which is based on the observed FUV spectral index $\beta \sim -2$ for high redshift galaxies. Note β is in defined in spectrum $f_{\lambda}d\lambda \propto \lambda^{\beta}d\lambda$, or $f_{\nu}d\nu \propto \nu^{-2-\beta}d\nu$, in the FUV spectral range. The accuracy of the normalization of our model is such that the model LF at $z = 6$ gives the same integrated light density as the observed one to the third digit.

Integrating the LF based on the Λ CDM model yield $\dot{N}_{\text{ion,int}}(z = 5.7) = 10^{51.6} \text{cMpc}^{-3} \text{s}^{-1}$, weakly dependent on M_{UV} lower limit. Dividing $\dot{N}_{\text{ion,IGM}}$ in Eq 1 by $\dot{N}_{\text{ion,int}}(z = 5.7)$ gives the mean luminosity-weighted escape fraction of Lyman continuum

$$f_{\text{esc},z=5.7} \equiv \frac{\dot{N}_{\text{ion,IGM}}}{\dot{N}_{\text{ion,int}}} = 10 \left(\frac{\dot{N}_{\text{ion,IGM}}}{10^{50.6} \text{cMpc}^{-3} \text{s}^{-1}} \right) \left(\frac{\xi_{\text{ion}}}{10^{25.2}} \right)^{-1} \% . \quad (14)$$

We will show in §4 how $\dot{N}_{\text{ion,IGM}}$ plays a key role in determining a lower bound on τ_e and how that in turn allow for a strong constraint on λ_{mfp} hence M_{cut} .

3. Reionization Histories Constrained by the State of IGM at $z = 5.7$

Any reionization history must satisfy the state of the IGM at $z = 5.7$ and the fact that the IGM is opaque to Ly α photon at just above that redshift. In this sense, the history of cosmological reionization becomes a boundary value problem, where we solve the evolution of HII volume fraction Q_{HII} with the following equation:

$$\frac{dQ_{\text{HII}}(z)}{dt} = \frac{\dot{N}_{\text{ion,IGM}}(z)}{n_{\text{H},0}} - \frac{Q_{\text{HII}}(z)}{t_{\text{rec}}(z)} , \quad (15)$$

where $n_{\text{H},0}$ is the comoving mean number hydrogen density, and

$t_{\text{rec}}(z) = [C_{\text{HII}}(z) \alpha_{\text{B}}(T) (1 + Y_{\text{p}}/4[1 - Y_{\text{p}}]) n_{\text{H},0} (1 + z)^3]^{-1}$ is the mean recombination time of ionized hydrogen in HII regions. Any solution to Eq 15 satisfies the following two boundary conditions:

$$f_{\text{esc}} \dot{N}_{\text{ion,int}} \bar{\sigma}_{\text{ion}} \lambda_{\text{mfp}}|_{z=5.7} = \dot{N}_{\text{ion,IGM}} \bar{\sigma}_{\text{ion}} \lambda_{\text{mfp}}|_{z=5.7} = 0.20_{-0.06}^{+0.11} \times 10^{-12} \text{s}^{-1} \quad (16)$$

and

$$Q_{\text{HII}}|_{z=5.7} = 1.0. \quad (17)$$

In Eq 15 at $z > 5.7$, since $\dot{N}_{\text{ion,int}}(z)$ is fixed by the Λ CDM model (see Figure 2), we are left with only one degree of freedom, namely, the evolution of f_{esc} with redshift. We model the redshift evolution of f_{esc} using a simple powerlaw form:

$$f_{\text{esc}}(z) = f_{\text{esc},z=5.7} \left(\frac{1+z}{6.7} \right)^{\chi} . \quad (18)$$

Note that $f_{\text{esc}}(z)$ in Eq 3, like $f_{\text{esc},z=5.7}$ in Eq 14, is averaged over all the galaxies at a given redshift; in other words, $f_{\text{esc}}(z)$ is the ratio of the total number of ionizing photons entering the IGM to the total number of ionizing photons produced. There is one additional physical process that is largely unconstrained by the state of the IGM at $z = 5.7$ but is important for the overall reionization history and integral electron scattering optical depth. That is, a change of IMF at some high redshift from regular Pop II stars to a perhaps more top-heavy and/or metal-free IMF, which may lead to a quantitative transition in ionizing photon production efficiency per unit

stellar mass, ϵ_{ion} . Thanks to our lack of knowledge with regard to this process, we choose to model ϵ_{ion} generally, albeit in a simple way, as

$$\epsilon_{\text{ion}} = \epsilon_{\text{ion,PopII}} + (\epsilon_{\text{ion,PopIII}} - \epsilon_{\text{ion,PopII}})H(\Omega_*[z] - \Omega_{\text{PopIII,crit}}), \quad (19)$$

where $\epsilon_{\text{ion,PopIII}}$ and $\epsilon_{\text{ion,PopII}}$ are ionizing photon production efficiency per unit stellar mass for Pop III and Pop II IMF, respectively. We adopt $\epsilon_{\text{ion,PopII}} = 3500$ photons/baryon and $\epsilon_{\text{ion,PopIII}} = 70000$ photons/baryon (e.g., Bromm et al. 2001), resulting in ratio of $\epsilon_{\text{ion,PopII}}/\epsilon_{\text{ion,PopIII}} = 20$, which enters our calculations. The transition between Pop III and Pop II is modeled by a smoothed Heavyside step function

$$H(\Omega_*[z] - \Omega_{\text{PopIII,crit}}) = (1 + \exp[-2(\Omega_*(z)/\Omega_{\text{PopIII,crit}} - 1)/\sigma_{\text{PopIII}}])^{-1}, \quad (20)$$

where $\Omega_*(z)$ is the amount of stars formed by redshift z computed in the Λ CDM model in units of critical density, $\Omega_{\text{PopIII,crit}}$, controls the transition from Pop III to Pop II when the amount of stars formed by some redshift in units of critical density has reached this value, and σ_{PopIII} controls the width of this transition in units of $\Omega_{\text{PopIII,crit}}$; when $\sigma_{\text{PopIII}} = 0$, one recovers the unsmoothed Heavyside step function. So far, we have three parameters to model the evolution of ionizing photon beyond $z = 5.7$, χ , $\Omega_{\text{PopIII,crit}}$ and σ_{PopIII} . As we will show later, the dependence of results on σ_{PopIII} is sufficiently weak that σ_{PopIII} can effectively be considered fixed, as long as its value is not too large. Therefore, we effectively have two free parameters in our model, χ and $\Omega_{\text{PopIII,crit}}$. Given that we have one equation, Eq 15, the general expectation is that there will be a family of solutions that will be able to meet the two boundary conditions, Eq 16, 17. Conversely, though, solving Eq 15 to obtain $Q_{\text{HII}}(z = 5.7) = 1$ does not necessarily result in an IGM at $z = 5.7$ that is consistent with the constraint imposed by the observations of Ly α optical depth, i.e., Eq 3, a point already noted by others (e.g., Robertson et al. 2013).

For each solution of $Q_{\text{HII}}(z)$, we compute the total electron scattering optical depth from $z = 0$ to recombination redshift z_{rec} by

$$\tau_e = \int_0^{z_{\text{rec}}} f_e(1 - f_s - f_n)Q_{\text{HII}}\sigma_{\text{TnH},0}[c/H(z)](1+z)^{-1}dz, \quad (21)$$

where f_e accounts for redshift evolution of helium contribution, we use $f_e = (0.76 + 0.24/0.76/4)$ for $z > 2.8$ and $f_e = (0.76 + 0.24/0.76/2)$ for $z \leq 2.8$, approximating He II reionization as a step function at $z = 2.8$, which is consistent with the observed He II absorption optical depth data of (Worseck et al. 2011), interpreted in the context of He II reionization simulations of (McQuinn et al. 2009). And f_s and f_n account for stellar density and neutral hydrogen density, respectively, which do not contribute to electron density. Wilkins et al. (2008) give $\Omega_*(z = 0) = 2.5 \times 10^{-3}$, while (Grazian et al. 2015) yield $\Omega_*(z = 6) = 3.7 \times 10^{-5}$. We interpolate between these two points to find an approximate stellar evolution fit as $\Omega_*(z) = 2.5 \times 10^{-3}(1+z)^{-2.1}$, translating to $f_s = 0.052(1+z)^{-2.1}$. Post-reionization most of the neutral hydrogen resides in DLAs and the observational data on the evolution of DLAs are available, albeit with significant errorbars. We approximate the data presented in Noterdaeme et al. (2009) by piece-wise powerlaws as follows: $\Omega_{\text{HI}} = 0.4 \times 10^{-3}$ at $z = 0$, which evolves linearly to $\Omega_{\text{HI}} = 0.9 \times 10^{-3}$ at $z = 0.5$,

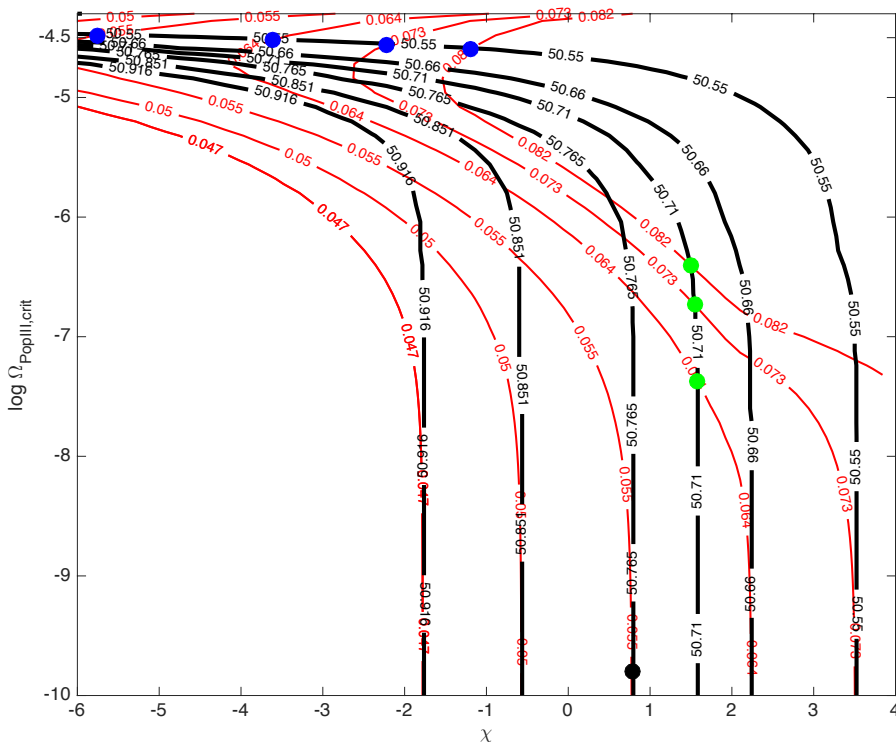


Fig. 3.— shows the contours of τ_e (red) and $\dot{N}_{\text{ion,IGM}}(z = 5.7)$ (black) in the $\chi - \Omega_{\text{PopIII,crit}}$ plane for $\sigma_{\text{PopIII}} = 0.25$. The red contours are labelled with τ_e values, whereas the black contours are labelled with $\log \dot{N}_{\text{ion,IGM}}(z = 5.7)$ values. The four blue solid dots indicate four possible solutions of $Q_{\text{HII}}(z)$ that yield total electron optical depths of $\tau_e = (0.055, 0.064, 0.073, 0.082)$, respectively, from left to right. The three green solid dots indicate another set of three possible solutions of $Q_{\text{HII}}(z)$ that yield total electron optical depths of $\tau_e = (0.082, 0.073, 0.064)$, respectively, from top to bottom. The black solid dot is a solution with $\tau_e = 0.055$. These specific solutions are discussed in the text.

which remains at $\Omega_{\text{HI}} = 0.9 \times 10^{-3}$ at $z = 0.5 - 3$, after which it linearly rises $\Omega_{\text{HI}} = 1.2 \times 10^{-3}$ at $z = 3.5$, followed by a constant $\Omega_{\text{HI}} = 1.2 \times 10^{-3}$ at $z = 3.5 - 5.7$.

Figure 3 shows the case with $\sigma_{\text{PopIII}} = 0.25$, to be examined in greater details. We have examined cases with $\sigma_{\text{PopIII}} = 0.5, 0.25, 0.05, 0.01$ and find that the results, as displayed in Figure 3 in terms of the contours, depend weakly on σ_{PopIII} . We note that the conclusions obtained are generic and more importantly, the solution family obtained that is still viable is very insensitive to the choice of σ_{PopIII} .

It proves useful for our discussion to rewrite one of the boundary value constraints, namely, Eq 16, as

$$\dot{N}_{\text{ion,IGM}}(z = 5.7) = (1.8 - 4.1) \times 10^{50} \left[\frac{\lambda_{\text{mfp}}(z = 5.7)}{7.6 \text{pMpc}} \right]^{-1} \text{cMpc}^{-3} \text{s}^{-1}, \quad (22)$$

where the range inside the first pair of parentheses on the right hand side corresponds to 1σ lower and upper limits of Eq 5. In this parameter space of $\chi - \Omega_{\text{PopIII,crit}}$ shown in Figure 3 we have solutions to Eq 15 that satisfy Eq 17, i.e., the universal reionization completes exactly at $z = 5.7$ with varying $\dot{N}_{\text{ion,IGM}}(z = 5.7)$ shown as the black contours. Superimposed as the red contours are values of τ_e for each solution.

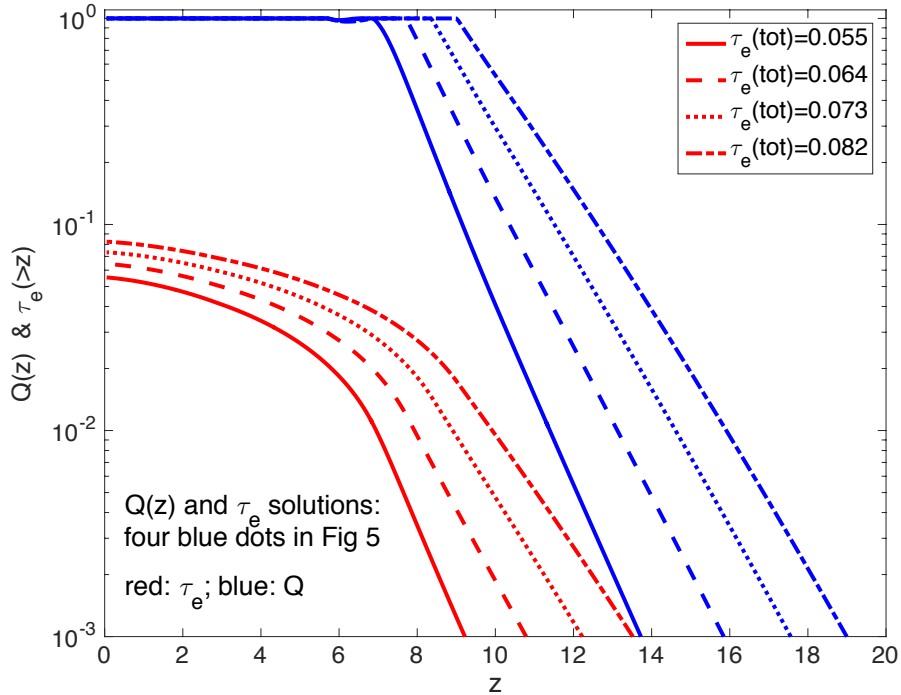


Fig. 4.— shows each of the four solutions of $Q_{\text{HII}}(z)$ (blue curves) indicated by the **four blue solid dots** in Figure 3, along with the respective cumulative τ_e (red curves).

It is now clear that the value of $\dot{N}_{\text{ion,IGM}}(z = 5.7)$ plays a key role in determining the viability of each solution of $Q_{\text{HII}}(z)$. Under the two boundary conditions, Eq 16 and 17, two families of solutions are possible, each of which is *simultaneously* consistent with the latest values of τ_e from Planck Collaboration et al. (2016) observations. Indicated by the **four blue dots** in Figure 3 are four solutions in the (we call) “Pop III-supported” family with $\tau_e = (0.055, 0.064, 0.073, 0.082)$ corresponding to the (central, $+1\sigma$, $+2\sigma$, $+3\sigma$) values from Planck Collaboration et al. (2016).

Figure 4 shows each of the four solutions of $Q_{\text{HII}}(z)$ (blue curves) indicated by the **four blue solid dots** in Figure 3, along with the respective cumulative τ_e (red curves). The common characteristics of these solutions in this solution family are that (1) $\chi < 0$, indicating that the escape fraction decreases with increasing redshift, (2) the Pop III stars make a significant and late contribution to the overall ionizing photon budget. The combination of negative χ and late, significant Pop III contribution permits a slight dip in ionized fraction at a redshift slightly higher

than $z = 5.7$, to satisfy 17. This set of solutions, however, may be inconsistent with some other independent observations. Here we provide some notable examples.

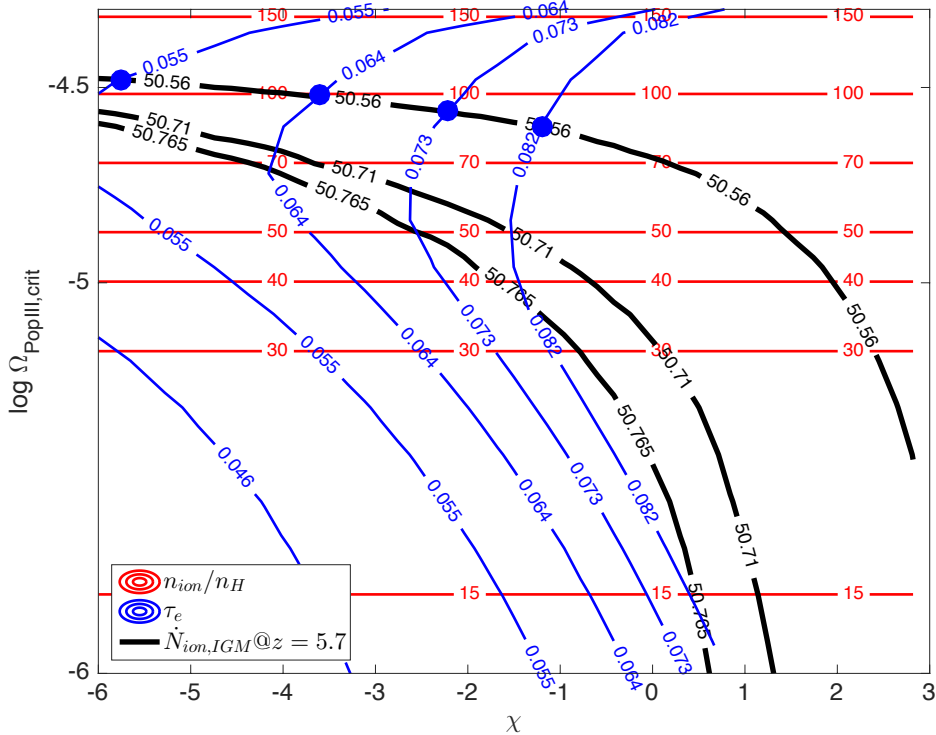


Fig. 5.— shows contours of the ratio of the number of ionizing photon produced per hydrogen atom (red), along with contours of τ_e (blue) and of $\log \dot{N}_{\text{ion,IGM}}(z = 5.7)$ (black).

Figure 5 shows contours of the ratio of the number ionizing photon produced per hydrogen atom (red). Fang & Cen (2004) perform a detailed analysis of metal enrichment history and show that Pop III to Pop II transition occurs when 3 – 20 ionizing photons per hydrogen atom, depending on the model for the IMF, have been produced by Pop III stars, based on considerations of primary atomic cooling agents, CII and OI, at low temperature, corresponding to $[\text{C}/\text{H}]_{\text{crit}} = -3.5$ and $[\text{O}/\text{H}]_{\text{crit}} = -3.1$ (Bromm & Loeb 2003). For the four solutions, indicated by the four blue dots in Figure 5, we see much higher, 80 – 110 ionizing photons per hydrogen atom have been produced at the model transition $\Omega_{\text{PopIII,crit}}$, in order to attain the solutions. Note that in the scenario of dust cooling induced fragmentation (Schneider & Omukai 2010), the critical transition metallicity is 1 – 3 orders of magnitude lower that is still more stringent. These considerations indicate that these $Q_{\text{HII}}(z)$ solutions are self-inconsistent, in the sense that the required Pop III contribution in order for the solutions to be possible is unattainable.

A second example concerns the neutral fraction of the IGM during the epoch of reionization at $z > 6$. In a recent careful analysis of possible signatures of damping wing absorption profiles of the $\text{Ly}\alpha$ emission line of quasar J1120+0641 at $z = 7.1$, under the assumption that DLAs, being sufficiently rare, are not responsible for the absorption of the $\text{Ly}\alpha$ emission

redward of the line, Greig et al. (2016) conclude that the mean neutral fraction of the IGM is $0.40^{+0.41}_{-0.32}$ (2σ). All of the four solutions shown in Figure 4 have the mean neutral fraction significantly less than a few percent, thus are ruled out at $> 2.5\sigma$ level.

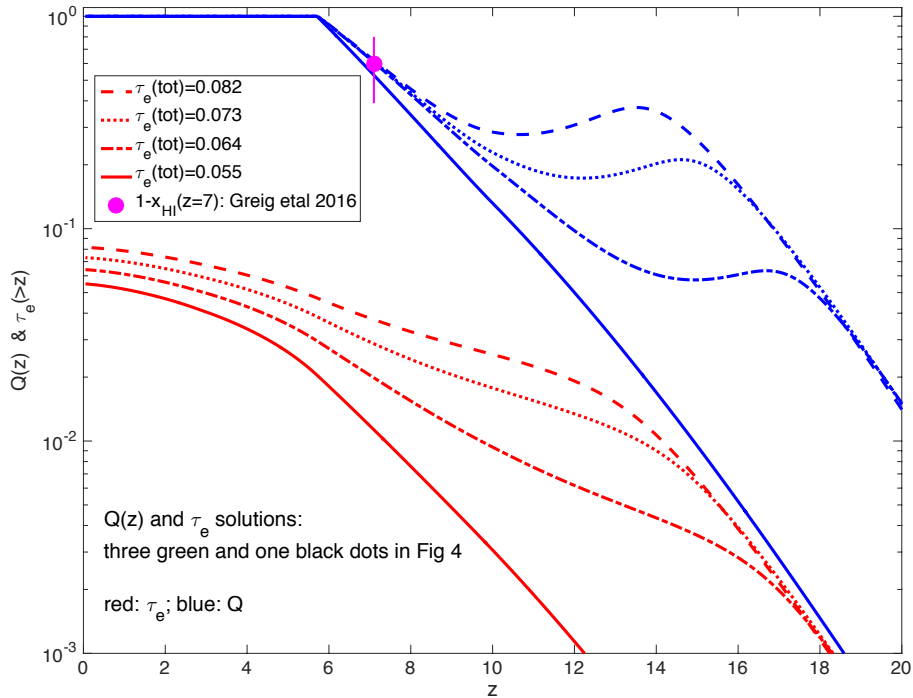


Fig. 6.— shows each of the four solutions of $Q_{\text{HII}}(z)$ (blue curves) indicated by the **three green** (for $\tau_e = (0.064, 0.074, 0.082)$) and one black (for $\tau_e = 0.055$) solid dots in Figure 3, along with the respective cumulative $\tau_e(> z)$ (red curves). Indicated by the magenta solid dot is an observational measurement of neutral fraction of the IGM at $z = 7.1$ by Greig et al. (2016) based on the damping wing signature imprinted on the red side of the Ly α emission line of quasar J1120+0641.

Let us now turn to the other solution family with reduced Pop III contribution that is additionally confined to much higher redshift. Figure 6 shows each of the three solutions of $Q_{\text{HII}}(z)$ (blue curves) indicated by the **three green** and one solid dots in Figure 3, along with the respective cumulative τ_e (red curves). Several trends shared by solutions in this solution family may be noted. First, $Q_{\text{HII}}(z)$ increases exponentially as a function of redshift in the range of $z = 5.7$ to $z = 9 - 14$, depending on the value of total τ_e ; a lower total τ_e corresponds to a higher redshift, but lower value of $Q_{\text{HII}}(z)$ base, from which the exponential growth starts. All four solutions are consistent with the observationally inferred mean neutral fraction of the IGM at $z = 7.1$, shown as a magenta dot with 1σ range (Greig et al. 2016). Second, there is a distinct, separate peak $Q_{\text{HII}}(z)$ at $z = 14 - 18$, for $\tau_e = 0.082 - 0.064$ (in that order) with height of $(0.4 - 0.07)$ (in the same order). This high redshift peak of $Q_{\text{HII}}(z)$ is due to contributions from Pop III stars. The exact height and duration of this peak may depend on the assumptions concerning the transition from Pop III to Pop II temporally and spatially, that will require

detailed modeling beyond the scope of this work. We note, however, that the results do not change significantly when values of $\sigma_{\text{III}} = 0.01 - 1$ are used (0.25 is used for the case shown in Figure 6), suggesting that the existence, the $Q_{\text{HII}}(z)$ value of the peak and the peak redshift are fairly robust. We also note that all these solutions lie below $\Omega_{\text{PopIII,crit}} = 10^{-6.4}$, which, when compared with Figure 5, indicates a consistency in terms of Pop III stars forming in the metallicity regime that is physically plausible, if low temperature atomic cooling, not dust cooling, dictates fragmentation of star-forming gas clouds. Finally, it is seen that these solutions have $\chi \geq 0$, indicating that the escape fraction increases with increasing redshift, perhaps not an unexpected result based on physical considerations that galaxies at high redshifts are less massive, their star-formation episodes more bursty and consequently their interstellar medium more porous to allow for more ionizing photons to escape. Simulation results are consistent with this trend (e.g., Kimm & Cen 2014). In summary, this solution family are self-consistent.

If, however, $\tau_e = 0.055$ holds up, there is no solution of $Q_{\text{HII}}(z)$ with $\log \dot{N}_{\text{ion,IGM}}(z = 5.7) = 50.71$. In order to get a solution with $\tau_e = 0.055$, one requires $\log \dot{N}_{\text{ion,IGM}}(z = 5.7) = 50.765$, which, with the conservative choice of $+1\sigma$ value $\Gamma_{-12} = 0.31$ (see Eq 5), in turn requires $\lambda_{\text{mfp}}(z = 5.7) = 5.3\text{pMpc}$, which would be at about 2.9σ lower bound of the observationally inferred value. In combination with the $+1\sigma$ value of Γ_{12} used, such an event would be a 3.0σ occurrence, suggesting tension, which we examine in the next section.

4. $\lambda_{\text{mfp}}(z = 5.7)$: A Strong Test of Matter Power Spectrum on Small Scales

We were left in a state of significant tension between accommodating $\tau_e = 0.055$ and $\lambda_{\text{mfp}}(z = 5.7)$ based on the extrapolated observational data at $z < 5.5$ in §3. The tension may be alleviated, if one chooses not to strongly advocate the central value of $\tau_e = 0.055$ (Planck Collaboration et al. 2016) but instead emphasize the harmonious concordance between $\lambda_{\text{mfp}}(z = 5.7)$, $\Gamma(z = 5.7)$ and $\tau_e \geq 0.64$. We take this discrepancy in a somewhat different way and suggest that the extrapolation of the lower redshift measurement of λ_{mfp} should be taken with caution, despite the smooth trend seen in the observed redshift range ($z = 2.3 - 5.5$). We take a step further yet to perform a theoretical analysis to better understand the physical origin of $\lambda_{\text{mfp}}(z = 5.7)$ in the context of the standard cosmological model.

It is useful to separate out the overall λ_{mfp} into two components in the post-overlap epoch at $z = 5.7$, one due to the “translucent”, general volume-filling low density IGM that collectively attenuates ionizing photons and the other due to “opaque” disks (like LLSs) that block entirely all incident ionizing photons. We shall denote them $\lambda_{\text{mfp,IGM}}$ and $\lambda_{\text{mfp,halo}}$, respectively. The total λ_{mfp} is

$$\lambda_{\text{mfp}} = (\lambda_{\text{mfp,halo}}^{-1} + \lambda_{\text{mfp,IGM}}^{-1})^{-1}. \quad (23)$$

The $\lambda_{\text{mfp,IGM}}$ can be approximated by the volume-weighted neutral fraction of the IGM as

$$\begin{aligned}\lambda_{\text{mfp,IGM}} &= (\bar{\sigma}_{\text{ion}} f_{\text{HI,vol}} n_{\text{H},0} (1+z)^3)^{-1} \\ &= 19.5 \left(\frac{1+z}{6.7}\right)^{-3} \left(\frac{\bar{\sigma}_{\text{ion}}}{3.16 \times 10^{-18} \text{cm}^2}\right)^{-1} \left(\frac{f_{\text{HI,vol}}}{0.9 \times 10^{-4}}\right)^{-1} \text{ pMpc},\end{aligned}\quad (24)$$

where $f_{\text{HI,vol}} = 0.9 \times 10^{-4}$ is the volume-weighted neutral fraction of the IGM, inferred by the directly observed Ly α (and higher order Lyman transitions) optical depth at $z = 5.7$ (Fan et al. 2006). As we have argued earlier, while the mass-weighted neutral fraction determined from such a method may be significantly model-dependent, the volume-weighted neutral fraction is not expected to be, because it is free from clumping factor dependence and most of the optical depth contributions stem from low-density regions of optical depth of order unity whose Jeans scales are typically resolved in most simulations used.

$\lambda_{\text{mfp,halo}}$ stems from self-shielding dense gas in halos. A computation of $\lambda_{\text{mfp,halo}}$ may not seem a well posed problem at first sight, because it would appear to depend on both the abundance of halos and their cross sections (the sizes of radiation blocking disks). It is not immediately obvious how one may precisely specify their cross sections, even if their abundance is known. We show that this ambiguity can be removed, when considerations are given to the physical conditions of halo gas as a function of halo-centric radius and a “correct” definition of $\lambda_{\text{mfp,halo}}$ is adopted, which we now describe.

After the HII regions have overlapped in the aftermath of reionization, neutral gas in halos essentially becomes a set of disconnected isolated islands that are increasingly self-shielded and optically thick to ionizing photons toward to the centers of halos. Under the assumption of spherical symmetry, for a given halo, we can compute the column density as a function of halo-centric radius r outside-in as

$$N_{\text{HI}}(r) = \int_r^\infty x_{\text{HI}}(r') \delta(r') n_{\text{H},0} (1+z)^3 dr', \quad (25)$$

where $\delta(r) \equiv n(r)/\bar{n}$ is overdensity, for which we use the universal halo density profile (NFW, Navarro et al. 1997) with gas following mass over the relevant radial range (e.g., Komatsu & Seljak 2001). In the core region of a halo the gas density is constrained such that the gas entropy does not fall below the entropy of the gas at the mean density and cosmic microwave background temperature. In practice, the upper limit of the integral in Eq 25 is chosen when $\delta = 1$ (i.e., the mean density) but its precise value makes no material difference to the calculated $N_{\text{HI}}(r)$ in the range of relevance. The local neutral fraction $x_{\text{HI}}(r)$ at radius r can be computed using the local balance between recombination and photoionization through a spherical radiative transfer:

$$\Gamma \exp[-N_{\text{HI}}(r) \bar{\sigma}_{\text{ion}}] x_{\text{HI}}(r) = [1 - x_{\text{HI}}(r)]^2 [1 + Y_p/4(1 - Y_p)] \alpha_B(T) \delta(r) n_{\text{H},0} (1+z)^3, \quad (26)$$

where Γ is the “background” ionization rate prior to significant attenuation when approaching the halo. We solve Eq (25,26) numerically to obtain $N_{\text{HI}}(r)$ and $x_{\text{HI}}(r)$, for a given Γ .

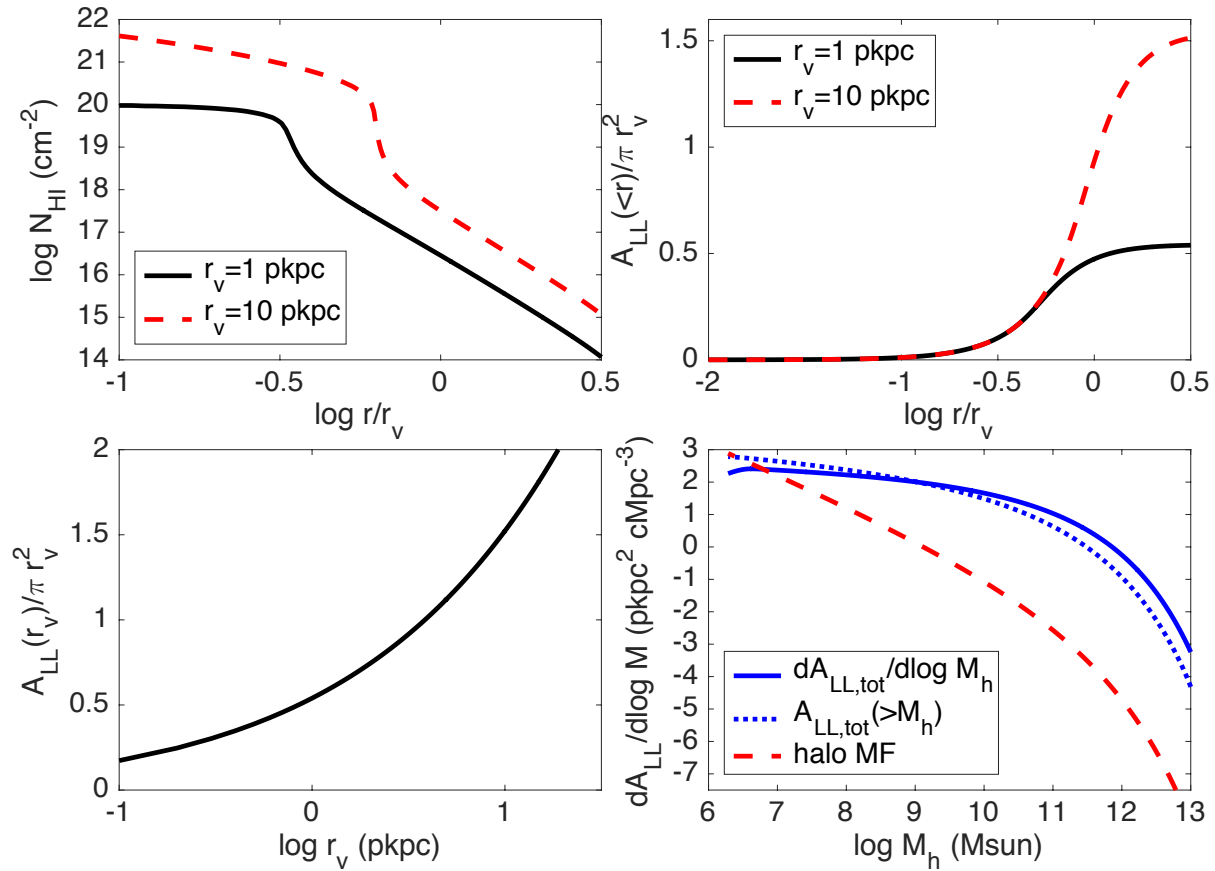


Fig. 7.— **Top-left panel:** shows the integrated column density (from outside inward down to the halo-centric radius r) as a function of r (in units of virial radius r_v), for two cases with virial radius r_v equal to 1 pkpc (black solid curve) and 10 pkpc (red dashed curve) at $z = 5.7$ [with corresponding virial (temperature, mass) of $(1.5 \times 10^3 \text{K}, 9.7 \times 10^6 M_\odot)$ and $(1.5 \times 10^5 \text{K}, 9.7 \times 10^9 M_\odot)$, respectively], using fiducial values for various parameters: $\Gamma_{-12} = 0.2$, $\bar{\sigma}_{\text{ion}} = 3.16 \times 10^{-18} \text{ cm}^2$. For the NFW profile we use a concentration parameter $C = 5$ in both cases. **Top-right panel:** shows the cumulative cross section for ionizing photons of a halo $A_{\text{LL}}(<r_p)$ in units of the virial area (πr_v^2) as a function of halo-centric radius in units of the virial radius r_v for the two halos shown in the top-left panel of Figure 7. **Bottom-left panel:** shown the effective total cross section for Lyman continuum photons in units of halo virial area as a function of halo virial radius at $z = 5.7$. **Bottom-right panel:** shows the differential function $dA_{\text{LL,tot}}/d \log M_h \equiv n(M_h)M \ln 10 A_{\text{LL}}(M_h)$ as a function of M_h (solid blue curve), its cumulative function $A_{\text{LL,tot}}(>M_h)$ (dotted blue curve), along with the halo mass function $n(M_h)M \ln 10$ as a function of M_h (dashed red curve).

In the top-left panel of Figure 7 we show the integrated column density (from outside inward down to the radius r) as a function of halo-centric radius r (in units of virial radius r_v) for two cases with virial radius r_v equal to 1 pkpc (black solid curve) and 10 pkpc (red dashed

curve), respectively. We see that at about $r/r_v \sim 3$ the column density is well below 10^{17}cm^{-2} , confirming that the exact integration starting radius is not important for column densities in the relevant range for significant attenuation of LyC photons. In both cases we also see that there is a rapid upturn of the column density starting around $\sim 10^{18} \text{cm}^{-2}$, indicating the radial location of the beginning of self-shield and transition from a highly ionized to an increasingly neutral medium. The rapid ascent suddely flattens out at $\sim 10^{20} \text{cm}^{-2}$, sigalling the arrival of a largely neutral medium, coincidental with column density similar to that of the damped Lyman alpha systems (DLAs). It is instructive to note that the transition from ionized to an increasingly neutral medium is halo virial radius (or halo mass) dependent, with a larger halo transitioning at a larger radius in units of its virial radius. This indicates that the density of the ionizing front propagating into halos is halo mass dependent, suggesting that the common practice of using a constant density as a proxy for the density of ionization front (e.g., Miralda-Escudé et al. 2000) could potentially be slightly extended, although a more detailed analysis should be performed to assess this.

To devise an appropriate method to compute the effective cross section A_{LL} for LyC photons for a given halo, it is useful to gain a more clear understanding of the physical meaning of $\lambda_{\text{mfp,halo}}$. For a line of sight cross area of size ΔA , if it is completely opaque to ionizing photons, then the effective area for intercepting LyC photons would be just equal to ΔA . For a cross area of size ΔA that is not completely opaque to LyC photons, one may define the effective area for intercepting ionizing photons ΔA_{LL} , which is

$$\Delta A_{LL} = \Delta A [1 - \exp(-N_{\text{HI}} \bar{\sigma}_{\text{ion}})], \quad (27)$$

where N_{HI} is the column density integrated along that line of sight (not the radially integrated column density shown in the top-left panel of Figure 7), which is computed using $N_{\text{HI}}(r)$ and $x_{\text{HI}}(r)$ that we have numerically obtained solving Eq (25,26).

Upon integrating the projected area of a halo, we obtain the cumulative cross section for ionizing photons of a halo as a function of projected radius r_p

$$A_{LL}(< r_p) = \int_0^{r_p} 2\pi r'_p [1 - \exp(-N_{\text{HI}}(r'_p) \bar{\sigma}_{\text{ion}})] dr'_p. \quad (28)$$

The top-right panel of Figure 7 shows $A_{LL}(< r_p)$ in units of the virial area (πr_v^2) as a function of halo-centric radius in units of the virial radius r_v for the two halos shown in the top-left panel of Figure 7. To re-iterate a point made earlier, the total effective cross section is larger for larger halos in units of the virial area, shown quantitatively in the bottom-left panel of Figure 7. In the calculations performed involving the NFW profile, one needs to specify the concentration parameter c , which has been computed by a number of groups (e.g., Bullock et al. 2001; Wechsler et al. 2002; Angel et al. 2016; Ricotti et al. 2007). We adopt the results of Dolag et al. (2004): $c = 9.6(M_h/10^{14} M_\odot)^{-0.10}(1+z)^{-1}$; the results obtained do not sensitively depend on slightly different formulae of c in the literature.

We compute $\lambda_{\text{mfp,halo}}$ by

$$\lambda_{\text{mfp,halo}}^{-1} = \int_{M_{\text{cut}}}^{\infty} n(M_{\text{h}}) M_{\text{h}} \ln 10 A_{\text{LL}}(M_{\text{h}}) d \log M_{\text{h}}, \quad (29)$$

where $A_{\text{LL}}(M_{\text{h}})$ is the total cross section of LyC photons for a halo of mass M_{h} ; $n(M_{\text{h}})$ is the halo mass function at the redshift in question. The bottom-right panel of Figure 7 shows cross section function, $n(M_{\text{h}}) M_{\text{h}} \ln 10 A_{\text{LL}}(M_{\text{h}})$ (solid blue curve), its cumulative function $A_{\text{LL,tot}}(> M_{\text{h}})$ (dotted blue curve), along with mass function, $n(M_{\text{h}}) M \ln 10$ (dashed red curve), as a function of M_{h} . We see that the cross section function is significantly flatter than the halo mass function, due to the fact that the cross section in units of virial area is higher with increasing halo mass, i.e., $A_{\text{LL}}(M_{\text{h}})/M_{\text{h}}^{2/3}$ correlates positively with M_{h} , shown in the bottom-left panel of Figure 7. Nonetheless, A_{LL} scales still sub-linearly with M_{h} , causing $n(M_{\text{h}}) M \ln 10 A_{\text{LL}}(M_{\text{h}})$ to increase with decreasing halo mass M_{h} .

The $\Gamma - \lambda_{\text{mfp}}$ relation in the standard ΛCDM model for four cases of $M_{\text{cut}} = (1.6 \times 10^8, 5.8 \times 10^7, 2.7 \times 10^7, 8.6 \times 10^6) M_{\odot}$, corresponding to a halo virial temperature cutoff of $T_{\text{v,cutoff}} = (10^4, 5 \times 10^3, 3 \times 10^3, 1.4 \times 10^3) \text{K}$, are shown also in Figure 1 as the blue curves. First of all our results affirm a general self-consistency between radiation field and ionization structures around halos in the ΛCDM model, since the theoretically predicted relation (the blue curves) can go through this already tightly constrained parameter space. This is a strong and unique support for the ΛCDM model with respect to its matter density power spectrum (both amplitude and shape) on small scales corresponding to halo masses approximately in the range of $10^7 - 10^{10} M_{\odot}$. It is noted that this constraint on matter power spectrum is based entirely on the consideration of the halos as “sinks” of ionizing photons. We point out the fact that $\lambda_{\text{mfp,halo}}$ depends sensitively on the lower mass cutoff M_{cut} in the integral in Eq 29, as shown in the bottom-right panel of Figure 7. We show that this dependence provides a new, sensitive probe of the small-scale power in the cosmological model, when confronted with measurements of τ_{e} . It is useful to note that in computing $\lambda_{\text{mfp,halo}}$ we have neglected possible contribution due to collisional ionization in halos with virial temperature significantly above 10^4K . Thus, our computed $\lambda_{\text{mfp,halo}}$ is somewhat overestimated and our subsequent conclusion drawn on small-scale power conservative.

Figure 8 shows λ_{mfp} as a function of the lower mass cutoff M_{cut} in the integral in Eq 29 (blue solid curve). Shown as symbols are four cases along the curve, with $(\log M_{\text{cut}}/M_{\odot}, \lambda_{\text{mfp}}/\text{pMpc}, \log \dot{N}_{\text{ion,IGM}}/\text{cMpc}^{-3}\text{s}^{-1}, \tau_{\text{e}})$ equal to $(5.10, 3.7, 50.916, 0.047)$ (green star), $(6.95, 5.3, 50.765, 0.055)$ (red dots), $(7.58, 6.8, 50.660, 0.064)$ (magenta square) and $(8.67, 10.5, 50.550, 0.073)$ (black diamond). Each set of four numbers has the following relational meaning: for a given measurement of τ_{e} , the minimum required ionizing photon emissivity entering the IGM is $\log \dot{N}_{\text{ion,IGM}}$ in order for that τ_{e} to be a possible solution, which in turn corresponds to a mean free path of λ_{mfp} , which can be achieved if the lower mass cutoff of the halo mass function is M_{cut} . We see that the dependence of λ_{mfp} on M_{cut} is significant, which provides a new constraint on the small-scale power in the cosmological model at a level that has hitherto been out of reach.

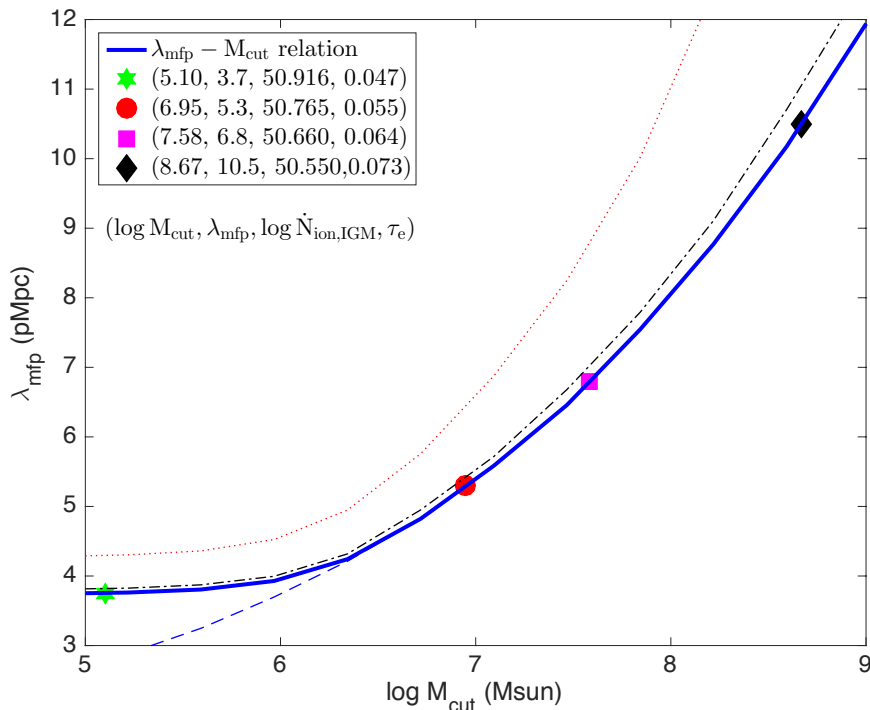


Fig. 8.— shows λ_{mfp} as a function of the lower mass cutoff M_{cut} in the integral in Eq 29 (blue solid curve). Also shown as symbols are four cases along the curve, with $(\log M_{\text{cut}}/M_{\odot}, \lambda_{\text{mfp}}/\text{pMpc}, \log \dot{N}_{\text{ion,IGM}}/c\text{Mpc}^{-3}\text{s}^{-1}, \tau_e)$ equal to (5.10, 3.7, 50.916, 0.047) (green star), (6.95, 5.3, 50.765, 0.055) (red dot), (7.58, 6.8, 50.660, 0.064) (magenta square) and (8.67, 10.5, 50.550, 0.073) (black diamond). The thin blue dashed line is obtained when no entropy floor due to that of mean cosmic gas is imposed. The thin, black dot-dashed and red dotted curves are obtained assuming there is no contribution from halos with virial temperature greater than $3 \times 10^5\text{K}$ and $3 \times 10^4\text{K}$, respectively

The dependence of λ_{mfp} on M_{cut} shown in Figure 8 can be translated into a constraint on dark matter particles. Here, we take warm dark matter as an example. In the warm dark matter model the smoothing scale, defined as the comoving half-wavelength of the mode for which the linear perturbation amplitude is suppressed by 2, is

$$R_s = 0.48(\Omega_M/0.25)^{0.11}(h/0.7)^{-1.22}(m_x/\text{keV})^{-1.11}h^{-1}\text{Mpc} \quad (30)$$

for a warm dark matter particle mass of m_x (e.g., Viel et al. 2005), which we adopt as a proxy for a sharp cutoff (or free-streaming scale of particles). The equivalent free-streaming halo mass is then

$$M_s = 5.8 \times 10^{10}(\Omega_M/0.3)^{1.33}(h/0.7)^{-4.66}(m_x/\text{keV})^{-3.33}M_{\odot}. \quad (31)$$

Given the dependence chain of $\log M_{\text{cut}}$ on λ_{mfp} on $\dot{N}_{\text{ion,IGM}}$ on τ_e , we obtain the lower bound on the mass m_x of thermally produced warm dark matter particles as a function of τ_e shown as

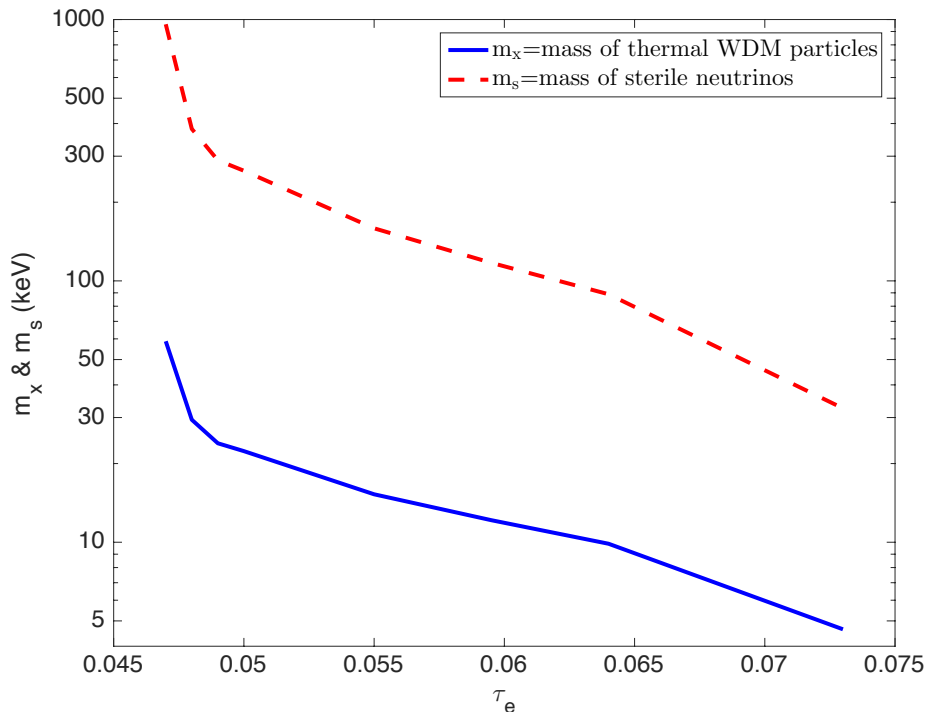


Fig. 9.— shows the lower bound on the mass m_x of thermally produced warm dark matter particles as a function of τ_e (blue solid curve). Similarly, the red dashed curve shows the lower bound on the mass m_s of sterile neutrinos as a function of τ_e .

the blue solid curve in Figure 9. The lower bound on the mass m_x of thermally produced warm dark matter particles can be translated similarly to a lower bound constraint on the mass m_s of sterile neutrinos produced via active-sterile neutrino oscillations obeying approximately a generalized Fermi-Dirac distribution. In this case, the effect of sterile neutrino is approximately the same as for thermally produced warm dark matter by using the following expression to relate the two masses (Colombi et al. 1996; Viel et al. 2005):

$$m_s = 4.46\text{keV} \left(\frac{m_x}{1\text{keV}} \right)^{4/3} \left(\frac{0.12}{\Omega_M h^2} \right)^{1/3}. \quad (32)$$

The result is shown as the red dashed curve in Figure 9.

The current best constraint on m_x based on Ly α forest is $m_x \geq 3.3\text{keV}(2\sigma)$ (Viel et al. 2013), improving upon earlier studies that generally constrain $m_x \geq 0.5 - 1\text{keV}$ (e.g., Narayanan et al. 2000; Barkana et al. 2001; Viel et al. 2005; Abazajian 2006). Combining with the 1σ upper limit used for Γ in our calculations, we find

$$m_x \geq (15.1, 9.8, 4.6)\text{keV at } (1, 1.4, 2.2\sigma) \text{ C.L.}, \quad (33)$$

based on $\tau_e = 0.055 \pm 0.009$ and $+1\sigma$ on Γ . The corresponding constraint on sterile neutrino mass is

$$m_s \geq (161, 90, 33)\text{keV at } (1, 1.4, 2.2\sigma) \text{ C.L.}, \quad (34)$$

which basically rules out, for example, 7keV sterile neutrino dark matter model (Bezrukov & Gorbunov 2014; Park et al. 2014; Abazajian 2014). The lower bound placed on warm dark matter particle mass (or in general, on the small-scale power) hinges on the assumption that dark matter halos make up the bulk of the Lyman limit systems at $z = 5.7$. Are there possible caveats with respect to this assumption? Let us examine this.

Under a physically plausible scenario of stellar reionization, there are possibly two additional kinds of (significantly) neutral systems to serve as Lyman limit systems to contribute to the absorption of LyC photons. The first kind is neutral regions that envelope the expanding HII regions. Let us suppose that each HII region that is expanding has a radius of R and the neutral region surrounding it has a thickness of ΔR . Analysis of the Ly α forest at $z = 5.7$ indicates a volume-weighted neutral fraction of the IGM $f_{\text{HI,V}} \sim 0.9 \times 10^{-4}$ at $z = 5.7$ (Fan et al. 2006). This provides a constraint on the possible size of ΔR :

$$\Delta R \leq \frac{f_{\text{HI,V}} R}{3}. \quad (35)$$

The ionization front propagation speed at $z = 5.7$ is

$$v_{\text{IF}} = \frac{F}{\bar{n}_{\text{H}}} = \frac{\Gamma}{\bar{\sigma} \bar{n}} = 1.7 \times 10^4 \left(\frac{\Gamma_{-12}}{0.31} \right) \left(\frac{\bar{\sigma}}{3.16 \times 10^{-18} \text{cm}^2} \right)^{-1} \text{km s}^{-1}, \quad (36)$$

where \bar{n}_{H} is mean hydrogen number density at $z = 5.7$. Thus, the time it takes to sweep through the radial shell of thickness ΔR would be

$$\Delta t = \frac{\Delta R}{v_{\text{IF}}} \leq \frac{f_{\text{HI,V}} R}{3 v_{\text{IF}}} = 9.4 \times 10^3 \left(\frac{R}{5.3 \text{pMpc}} \right) \left(\frac{f_{\text{HI,V}}}{0.9 \times 10^{-4}} \right) \left(\frac{\Gamma_{-12}}{0.31} \right)^{-1} \left(\frac{\bar{\sigma}}{3.16 \times 10^{-18}} \right) \text{yrs}. \quad (37)$$

Thus, for any reasonable values of the parameters involved, Δt is much shorter than the Hubble time at $z = 5.7$ (which is about 1 Gyr). This suggests that such a configuration is highly unlikely. Note that our assumption that these shells surround spherical HII regions is not necessary but only for the ease of illustration. If these spherical shells are replaced by pancake bridges or filamentary bridges between (or connecting) HII regions, the results and conclusions based on the above analysis remain largely the same, as long as the size of these pancakes or filaments are on the same order of $\sim 10 \text{pMpc}$; in terms of our conclusion reached, even for a size of 1000pMpc , our conclusion remains unchanged.

The second kind of possible neutral regions may be comprised of patches of neutral islands in the voids that are last reionized. We approximate them as opaque spheres with a radius of r_{void} and a mean separation between them of d_{void} , which can be related to the observed $f_{\text{HI,V}}$:

$$\frac{4\pi}{3} r_{\text{void}}^3 d_{\text{void}}^{-3} \leq f_{\text{HI,V}}. \quad (38)$$

The mean free path to LyC photons due to these islands would be

$$\lambda_{\text{mfp,void}} = \frac{d_{\text{void}}^3}{\pi r_{\text{void}}^2} \geq \left(\frac{4}{3} \right)^{2/3} \pi^{-1/3} d_{\text{void}} f_{\text{HI,V}}^{-2/3} = 412 d_{\text{void}} \left(\frac{f_{\text{HI,V}}}{0.9 \times 10^{-4}} \right)^{-2/3}. \quad (39)$$

The typical separations of voids, i.e., d_{void} , has to be on the order of the clustering scale of galaxies, which is about $4 - 5\text{cMpc}$ (e.g., Ouchi et al. 2010), or larger. This suggests that $\lambda_{\text{mfp,void}} \geq 245 \text{ pMpc}$ at $z = 5.7$, implying that possible, to-be-last-reionized neutral islands in voids do not contribute much to the mean free path of LyC photons at $z = 5.7$.

We thus conclude that halos likely contribute predominantly to the mean free path of LyC photons at $z = 5.7$ (likely at all lower redshifts as well, for that matter). Finally, we note that for simplicity we have adopted the assumption of sphericity of gas distribution in and around halos in question. Any deviation from sphericity would result in a reduction in cross section hence a more stringent demand for more small scale power. In addition, we note that baryonic fraction may be lower than the mean universal fraction. Furthermore, some gas in large halos with virial temperature higher than $\sim 10^4\text{K}$ may be heated up to remove itself from the HI category. To give a sense of the magnitude of this effect we show in Figure 8 two additional cases where we assume that halos with virial temperature greater than $3 \times 10^5\text{K}$ (thin, black dot-dashed curve) and $3 \times 10^4\text{K}$ (thin red dotted curve), respectively, do not contribute to λ_{mfp} . We see a significant effect; numerically, to attain $\lambda_{\text{mfp}} = (5.3, 6.8, 10.5)\text{pMpc}$ in order to yield $\tau_e = (0.047, 0.055, 0.064, 0.073)$, respectively, the required $\log M_{\text{cut}}$ changes from $(8.67, 7.58, 6.95)$ for no upper cutoff to $(8.54, 7.51, 6.89)$ for upper cutoff of virial temperature of $3 \times 10^5\text{K}$, to $(7.92, 7.07, 6.51)$ for upper cutoff of virial temperature of $3 \times 10^4\text{K}$. Moreover, internal ionizing radiation may reduce the HI fraction. Therefore, our assumptions and derived limits on small-scale power and on dark matter particle mass are all on the conservative side.

5. Discussion

5.1. Rapid Reionization Towards $z = 5.7$

The intrinsic emissivities of LyC photons at $z = 5.7$ and $z = 6$ are almost identical. We can use this fact to outline the nature of percolation of HII regions near the end of the reionization. We first note that we find that the theoretically derived relation of $\Gamma - \lambda_{\text{mfp}}$ at $z = 6$ is nearly identical to that at $z = 5.7$ at the visual resolution of eye when overplotted in Figure 1. It means, if the universe were in the post-overlap regime already at $z = 6$, its volume-weighted neutral fraction ought to be similar to that at $z = 5.7$. In other words, λ_{mfp} due to halos (mostly) based on ΛCDM model and emissivity at $z = 6$ can easily accommodate a transparent universe similar to the one observed at $z = 5.7$. The observations indicate otherwise: $f_{\text{HI,V}} \sim 0.9 \times 10^{-4}$ at $z = 5.7$ versus $f_{\text{HI,V}} > 2 \times 10^{-4}$ at $z = 6$ (Fan et al. 2006). Thus, the universe is not fully ionized at $z = 6$ in the way of imposing a smaller λ_{mfp} hence a lower Γ for a given $\dot{N}_{\text{ion,IGM}}$. The likely, perhaps only, consistent solution would be that HII regions have not overlapped at $z = 6$ so that neutral patches in the IGM (not in the halos) render λ_{mfp} much lower than the notional $\lambda_{\text{mfp,IGM}}$ and $\lambda_{\text{mfp,halo}}$ in the post-overlap epoch. The inferred value of $\Gamma_{-12} < 0.02$ at $z = 6$ (based on Ly γ absorption) (Cen & McDonald 2002; Fan et al. 2006) suggests that λ_{mfp} at $z = 6$ is an order of magnitude lower than that at $z = 5.7$.

This is clear and fairly direct evidence that the percolation of HII regions is not yet complete at $z = 6$, indicating that the universe is in a rapid transitory phase from $z = 6$ to $z = 5.7$ clearing up some of the last neutral patches that dominate the mean free path, in a monotonic and irreversible process. Topologically, this indicates that HII regions transition from a set of isolated islands at $z = 6$ to a connected network of swiss-cheese-like HII region at $z = 5.7$.

This expected rapid reionization process is consistent with and required by the necessary small values of $\lambda_{\text{mfp}} \leq 6.8 \text{pMpc}$ at $z = 5.7$ to achieve $\tau_e \leq 0.064$, which in turn requires contribution from minihalos (those with virial temperature less than 10^4K or virial mass less than $1.6 \times 10^8 M_\odot$ at $z = 5.7$). Gas in minihalo, when exposed to ionizing photons, responds dynamically by slowly evaporating through the action of thermal pressure of photoheated gas. Iliev et al. (2005) show that it takes about 100 – 200 Myr to photoevaporate a minihalo of mass $10^7 M_\odot$ at $z = 9$. This process is expected to take longer for more massive minihalos. In our case, a minihalo of mass $10^7 M_\odot$ is relevant for $\tau_e = 0.055$ (see the red dot in Figure 8); for $\tau_e = 0.064$ minihalos of mass $1.6 \times 10^8 M_\odot$ would be relevant (see the magenta square in Figure 8). Thus, it is probably true that, for the range of interest, the time scale taken for photoevaporation of relevant minihalos is 100 – 200 Myr or longer. We note that the universal age difference from $z = 6$ to $z = 5.7$ is 63 Myr, from $z = 7$ to $z = 5.7$ is 231 Myr. We see in Figure 6 that the neutral fraction at $z = 7$ is about 40%, meaning about 40% of minihalos have not yet been exposed to ionizing radiation at $z = 7$. Thus, it is probable that a significant fraction, perhaps a large majority, of minihalos have not lost gas in their inner regions (that actually contribute to the mean free path of LyC photons) by $z = 5.7$, permitting the possibility that they contribute significantly to the mean free path of LyC photons, if necessary.

5.2. On f_{esc} of Galaxies at Epoch of Reionization

Using Eq 14, the four points (represented by the four symbols) in Figure 8 give $f_{\text{esc}} = (20.7, 14.6, 11.5, 8.9)\%$, in order to arrive at the reionization solutions constrained by the state of the IGM at $z = 5.7$ with $\tau_e = (0.047, 0.055, 0.064, 0.073)$, respectively.

This required f_{esc} based on the observed state of the IGM at $z = 5.7$ is consistent with computed $f_{\text{esc,comp}} = 10 - 14\%$ based on state-of-the-art high resolution cosmological radiation hydrodynamic simulations of dwarf galaxies at the epoch of reionization of Kimm & Cen (2014). We point out that the upper value (14%) includes contributions from runaway OB stars. It is noteworthy that $f_{\text{esc,comp}}$ is effectively a measure of the porosity of the interstellar medium, where LyC photons escape through transparent holes into the IGM. Therefore, a correct treatment/implementation of supernova feedback is essential, as is in Kimm & Cen (2014) but not in any other simulations that the author is aware of. Including Wolf-Rayet stars for Pop II stellar population, which empirically are much more abundant in local metallicity environment that is expected for galaxies at the epoch of reionization, may further increase the ratio of LyC photons to FUV photons, i.e., ξ_{ion} , thus lessen the requirement for a high f_{esc} . Thus, it seems that

the stellar emissivity observed is adequate for maintaining the state of the IGM in terms of global and local ionization balance. It should be noted that these changes have no effect on solutions of reionization history that we have obtained, which depends directly on $\dot{N}_{\text{ion,IGM}}$.

5.3. Dichotomy in the Evolution of Lyman Alpha Emitters $z > 6$

In Figure 3 we see that solutions without Pop III contributions require $\chi = (0.7, 2.2, 3.6)$ for $\tau_e = (0.055, 0.064, 0.073)$, respectively. In general, the solutions even with Pop III contributions requires $\chi > 0$ as long as $\tau_e \geq 0.052$. We note that the overall f_{esc} tends to correlate with the porosity of the ISM, while individual f_{esc} is strongly dependent on the line of sight of the observer (e.g., Cen & Kimm 2015). A positive $\chi > 0$ is physically consistent with the expectation that smaller galaxies, having shallower gravitational potential wells, may be more susceptible to feedback processes from supernovae and have more porous ISM. Simulation results are consistent with this expected trend (e.g., Kimm & Cen 2014).

Is there observational evidence that the escape of Ly α and of LyC photons are both correlated with ISM porosity? Jones et al. (2013) find an interesting trend of lower covering fractions of low-ionization gas for galaxies with strong Ly α emission, providing evidence for a reduction in the average HI covering fraction (hence an increase in the escape fraction of ionizing radiation) is correlated with increase in Ly α emission. Shapley et al. (2003) find that the blueshifts of interstellar absorption lines in LAEs and LBGs are similar at $\sim -200 \text{ km s}^{-1}$, suggesting that the velocity of outflows in LAEs and LBGs are comparable. But their study also reveals a trend that Ly α EW increases with decreasing $\Delta v_{\text{em-abs}}$ in the EW range of -15 to $+50 \text{ \AA}$. Furthermore, they confirm that $\Delta v_{\text{Ly}\alpha}$ of LAEs is systematically smaller than the values of LBGs, with $\Delta v_{\text{Ly}\alpha}$ of about 200 km s^{-1} for LAEs compared to about 400 km s^{-1} for LBGs. Moreover, they clarify that $\Delta v_{\text{Ly}\alpha}$ decreases with increasing EW of Ly α . Recently, Shibuya et al. (2014) find an anti-correlation between Ly α EW and the covering fraction estimated from the depth of absorption lines, which is an indicator of average neutral hydrogen column density. Their results support the idea that neutral column density is a key quantity determining Ly α emissivity, consistent with the notion that the escape of LyC and Ly α is correlated with each other and due to lower column density holes in the ISM. The combination of these facts leads one to conclude that the Ly α velocity offset is positively correlated with N_{HI} and negatively correlated with EW, exactly predicted from results based on Ly α radiative transfer calculations (e.g., Zheng et al. 2010). None of these properties concerning Ly α emission can be attributed to differences in the outflow velocity, which do not appear to exist between LAEs and LBGs. Taken together, intrinsically, one would have expected then that the escape of Ly α photons should be made easier with increasing redshift; i.e., both the ratio of Lyman alpha emitters to overall galaxy population at a chosen Ly α EW or the overall Ly α luminosity to FUV luminosity ratio as a whole are expected to increase with redshift beyond $z = 5.7$.

Such an expectation is not borne out with observations. At some EW cuts, observations

have consistently found that the fraction of LAEs out of LBGs decreases by a significant factor from redshift $z = 6$ to $z = 8$ (e.g., Treu et al. 2013; Vanzella et al. 2014; Faisst et al. 2014; Schenker et al. 2014; Tilvi et al. 2014; Furusawa et al. 2016). This observational evidence strongly suggests that the intergalactic medium may have increasingly diminished the observability of the Ly α from $z \sim 6$ to $z \sim 8$, consistent with the rapid reionization picture depicted in Figure 6). Physically, this is due to the fact that significantly neutral IGM limits the size of Stromgren sphere around galaxies (Cen & Haiman 2000). Caruana et al. (2014) conclude that the neutral fraction of the IGM at $z \sim 7$ to be ~ 0.5 , which would be consistent with our computed model shown in Figure 6).

On the other hand, even if the IGM is indeed masking the appearance of the Ly α emission for most, relatively low luminosity galaxies at the epoch of reionization, for rare, very luminous galaxies (which each are also likely clustered with other galaxies) with large Stromgren spheres, their Ly α emission lines may be unaffected or possibly enhanced (given $\chi > 0$), under suitable conditions. A corroborative or confirmative piece of evidence for this may be that, if a strong Ly α line is detected, the emission region could, but not necessarily required to, be compact spatially and in velocity space due to lack of scattering. There are observational indications that this may in fact be the case. Sobral et al. (2015) observe a luminous Ly α source (CR7) with luminosity of $10^{43.93 \pm 0.05}$ erg/s at $z = 6.6$ (the most luminous Ly α emitter ever found at $z > 6$) but with a narrow FWHM of 266 ± 15 km s $^{-1}$. Hu et al. (2016) detect a luminous Ly α emitting galaxy, COLA1, with luminosity of $10^{43.9}$ erg/s at $z = 6.593$. COLA1 shows a multi-component Ly α profile with a blue wing, suggesting a large and highly Stromgren sphere perhaps well extending into the infall region. Matthee et al. (2015) have argued that there is little evolution in the luminosity function of the most luminous LAEs at these redshifts, suggesting that these objects lie in large HII regions and protect themselves from changes in IGM neutral fraction, consistent with the expectation, at least in principle. More pinpointed analysis will be desirable in this respect, combining reionization simulations with detailed radiative transfer of Ly α photons.

In summary, we expect that there is a dichotomy in the evolution of Ly α emitting galaxies. For relatively low Ly α luminosity galaxies, their emission lines will be progressively diminished with increasing redshift due to the increasingly neutral IGM beyond $z \sim 6$. On the other hand, for the most luminous Ly α emitters, under suitable conditions, their Stromgren spheres are large enough to allow their Ly α line to escape unscathed by the neutral IGM. Both are consistent with present tentative observational evidence.

6. Conclusions

We utilize the joint observations of the Ly α forest, the mean free path of ionizing photons λ_{mfp} , the luminosity function of galaxies and the total electron scattering optical depth τ_e , and theoretical insight on a relation between matter power spectrum and λ_{mfp} , to perform a detailed

analysis of the solutions of cosmic reionization history that satisfy the observed boundary conditions of the IGM at $z = 5.7$. We summarize results and conclusions.

(1) A theoretical relation between the mean free path and ionization rate at $z = 5.7$, requiring only the matter power spectrum, is derived. More scale power on $10^6 - 10^9 M_\odot$ scales leads to lower mean free path.

(2) A negative relation is found between the minimum effective ionizing photon emissivity for the IGM at $z = 5.7$ and the electron scattering optical depth τ_e . A higher emissivity is coupled with a less steep increase of ionizing photon escape fraction with increasing redshift, resulting in a later reionization episode hence a lower τ_e .

(3) The minimum required mean escape fraction of ionizing photons from galaxies at $z = 5.7$ is found to be $f_{\text{esc}} = (20.7, 14.6, 11.5, 8.9) \left(\frac{\xi_{\text{ion}}}{10^{25.2}}\right)^{-1} \%$ for $\tau_e = (0.047, 0.055, 0.064, 0.073)$, respectively, where ξ_{ion} is the ratio of ionizing photo production rate (in $\text{cMpc}^{-3} \text{s}^{-1}$) to FUV spectral density (in $\text{erg s}^{-1} \text{Hz}^{-1} \text{cMpc}^{-3}$). The escape fraction is predicted to increase with increasing redshift, with the rate of increase required higher for higher τ_e .

(4) While there is a family of possible solution, the 50% ionization fraction redshift lies in a relatively narrow range of $z = 6.5 - 7.5$ for $\tau_e = 0.050 - 0.082$. The late reionization suggests that relatively low luminosity $\text{Ly}\alpha$ emitters beyond $z = 6$, incapable of carving out a sufficiently large Stromgren sphere, will be increasingly diminished, although the most luminous $\text{Ly}\alpha$ emitters may possess a large enough Stromgren sphere to allow unimpeded transmission of their $\text{Ly}\alpha$ lines, possibly characterized by compact spatial or velocity extent.

(5) Topologically, reasonable arguments lead to the picture that the universe transitions from a set of isolated HII bubbles of typical individual sizes probably no greater than 1pMpc at $z = 6$ to a set of isolated neutral islands centered on halos that are embedded in one connected of HII region at $z = 5.7$.

(6) A positive relation is found between τ_e and the maximum mean free path of ionizing photons at $z = 5.7$. The outcome comes about because the product of the free path and emissivity of ionizing photons at $z = 5.7$ is constrained by the observed Gunn-Peterson optical depth. The maximum mean free path at $z = 5.7$ is $(3.7, 5.3, 6.8, 10.5)\text{pMpc}$ in order to yield $\tau_e = (0.047, 0.055, 0.064, 0.073)$, respectively. We do not find it possible to find a reionization solution with $\tau_e < 0.047$ that satisfies all observed conditions.

(7) The electron scattering optical depth τ_e thus provides a constraint on the mean free path, which in turn yields a new and powerful constraint on the matter power spectrum on $10^6 - 10^9 M_\odot$ scales at $z = 5.7$. With the latest Planck measurements of $\tau_e = 0.055 \pm 0.009$, we can place an upper limit of $(8.9 \times 10^6, 3.8 \times 10^7, 4.2 \times 10^8) M_\odot$ on the cutoff mass of the halo mass function, or equivalent a lower limit on warm dark matter particle mass $m_x \geq (15.1, 9.8, 4.6)\text{keV}$ or on sterile neutrino mass $m_s \geq (161, 90, 33)\text{keV}$ in the warm dark matter model, at $(1, 1.4, 2.2)\sigma$ confidence level.

(8) It is clear that a solution to the missing satellite problem (Klypin et al. 1999; Moore

et al. 1999) is unattainable via the route of warm dark matter particle origin, because of the strong constraint on the upper bound on dwarf halo mass of $\leq 4.2 \times 10^8 M_{\odot}$ at 2.2σ found.

I thank Xiaohui Fan, Jordi Miralda-Escude, Graca Rocha and Hy Trac for helpful discussion. I also thank an anonymous referee for useful and constructive comments. This work is supported in part by grants NNX12AF91G and AST15-15389.

REFERENCES

- Abazajian, K. 2006, *Phys. Rev. D*, 73, 063513
- Abazajian, K. N. 2014, *Physical Review Letters*, 112, 161303
- Angel, P. W., Poole, G. B., Ludlow, A. D., Duffy, A. R., Geil, P. M., Mutch, S. J., Mesinger, A., & Wyithe, J. S. B. 2016, *MNRAS*, 459, 2106
- Barkana, R., Haiman, Z., & Ostriker, J. P. 2001, *ApJ*, 558, 482
- Becker, G. D., Rauch, M., & Sargent, W. L. W. 2007, *ApJ*, 662, 72
- Bezrukov, F. L., & Gorbunov, D. S. 2014, *Physics Letters B*, 736, 494
- Bouwens, R. J., Illingworth, G. D., Oesch, P. A., Trenti, M., Labbé, I., Bradley, L., Carollo, M., van Dokkum, P. G., Gonzalez, V., Holwerda, B., Franx, M., Spitler, L., Smit, R., & Magee, D. 2015, *ApJ*, 803, 34
- Boylan-Kolchin, M., Bullock, J. S., & Kaplinghat, M. 2011, *MNRAS*, 415, L40
- Bromm, V., Kudritzki, R. P., & Loeb, A. 2001, *ApJ*, 552, 464
- Bromm, V., & Loeb, A. 2003, *ApJ*, 596, 34
- Bullock, J. S., Kolatt, T. S., Sigad, Y., Somerville, R. S., Kravtsov, A. V., Klypin, A. A., Primack, J. R., & Dekel, A. 2001, *MNRAS*, 321, 559
- Caruana, J., Bunker, A. J., Wilkins, S. M., Stanway, E. R., Lorenzoni, S., Jarvis, M. J., & Ebert, H. 2014, *MNRAS*, 443, 2831
- Cen, R., & Haiman, Z. 2000, *ApJ*, 542, L75
- Cen, R., & Kimm, T. 2015, *ApJ*, 801, L25
- Cen, R., & McDonald, P. 2002, *ApJ*, 570, 457
- Cen, R., Miralda-Escude, J., Ostriker, J. P., & Rauch, M. 1994, *ApJ*, 437, L9
- Colombi, S., Dodelson, S., & Widrow, L. M. 1996, *ApJ*, 458, 1

- Dijkstra, M., Wyithe, J. S. B., & Haiman, Z. 2007, *MNRAS*, 379, 253
- Dolag, K., Bartelmann, M., Perrotta, F., Baccigalupi, C., Moscardini, L., Meneghetti, M., & Tormen, G. 2004, *A&A*, 416, 853
- Faisst, A. L., Capak, P., Carollo, C. M., Scarlata, C., & Scoville, N. 2014, *ApJ*, 788, 87
- Fan, X., Narayanan, V. K., Strauss, M., White, R. L., Becker, R. H., Pentericci, L., & Rix, H.-W. 2002, *AJ*, 123, 1247
- Fan, X., Strauss, M. A., Becker, R. H., White, R. L., Gunn, J. E., Knapp, G. R., Richards, G. T., Schneider, D. P., Brinkmann, J., & Fukugita, M. 2006, *AJ*, 132, 117
- Fang, T., & Cen, R. 2004, *ApJ*, 616, L87
- Finlator, K., Oh, S. P., Özel, F., & Davé, R. 2012, *MNRAS*, 427, 2464
- Furusawa, H., Kashikawa, N., Kobayashi, M. A. R., Dunlop, J. S., Shimasaku, K., Takata, T., Sekiguchi, K., Naito, Y., Furusawa, J., Ouchi, M., Nakata, F., Yasuda, N., Okura, Y., Taniguchi, Y., Yamada, T., Kajisawa, M., Fynbo, J. P. U., & Le Fevre, O. 2016, *ArXiv e-prints*
- Gnedin, N. Y., & Ostriker, J. P. 1997, *ApJ*, 486, 581
- Grazian, A., Fontana, A., Santini, P., Dunlop, J. S., Ferguson, H. C., Castellano, M., Amorin, R., Ashby, M. L. N., Barro, G., Behroozi, P., Boutsia, K., Caputi, K. I., Chary, R. R., Dekel, A., Dickinson, M. E., Faber, S. M., Fazio, G. G., Finkelstein, S. L., Galametz, A., Giallongo, E., Giavalisco, M., Grogin, N. A., Guo, Y., Kocevski, D., Koekemoer, A. M., Koo, D. C., Lee, K.-S., Lu, Y., Merlin, E., Mobasher, B., Nonino, M., Papovich, C., Paris, D., Pentericci, L., Reddy, N., Renzini, A., Salmon, B., Salvato, M., Sommariva, V., Song, M., & Vanzella, E. 2015, *A&A*, 575, A96
- Greig, B., Mesinger, A., Haiman, Z., & Simcoe, R. A. 2016, *ArXiv e-prints*
- Gunn, J. E., & Peterson, B. A. 1965, *ApJ*, 142, 1633
- Haiman, Z., & Cen, R. 2005, *ApJ*, 623, 627
- Hinshaw, G., Larson, D., Komatsu, E., Spergel, D. N., Bennett, C. L., Dunkley, J., Nolte, M. R., Halpern, M., Hill, R. S., Odegard, N., Page, L., Smith, K. M., Weiland, J. L., Gold, B., Jarosik, N., Kogut, A., Limon, M., Meyer, S. S., Tucker, G. S., Wollack, E., & Wright, E. L. 2013, *ApJS*, 208, 19
- Hu, E. M., Cowie, L. L., Songaila, A., Barger, A. J., Rosenwasser, B., & Wold, I. 2016, *ArXiv e-prints*
- Iliev, I. T., Mellema, G., Pen, U.-L., Merz, H., Shapiro, P. R., & Alvarez, M. A. 2006, *MNRAS*, 369, 1625

- Iliev, I. T., Shapiro, P. R., & Raga, A. C. 2005, *MNRAS*, 361, 405
- Jones, T. A., Ellis, R. S., Schenker, M. A., & Stark, D. P. 2013, *ApJ*, 779, 52
- Kimm, T., & Cen, R. 2014, *ApJ*, 788, 121
- Klypin, A., Kravtsov, A. V., Valenzuela, O., & Prada, F. 1999, *ApJ*, 522, 82
- Komatsu, E., & Seljak, U. 2001, *MNRAS*, 327, 1353
- Madau, P., Haardt, F., & Rees, M. J. 1999, *ApJ*, 514, 648
- Matthee, J., Sobral, D., Santos, S., Röttgering, H., Darvish, B., & Mobasher, B. 2015, *MNRAS*, 451, 400
- McQuinn, M., Lidz, A., Zaldarriaga, M., Hernquist, L., Hopkins, P. F., Dutta, S., & Faucher-Giguère, C. 2009, *ApJ*, 694, 842
- Mesinger, A., Haiman, Z., & Cen, R. 2004, *ApJ*, 613, 23
- Miralda-Escudé, J., Haehnelt, M., & Rees, M. J. 2000, *ApJ*, 530, 1
- Moore, B., Ghigna, S., Governato, F., Lake, G., Quinn, T., Stadel, J., & Tozzi, P. 1999, *ApJ*, 524, L19
- Narayanan, V. K., Spergel, D. N., Davé, R., & Ma, C. 2000, *ApJ*, 543, L103
- Navarro, J. F., Frenk, C. S., & White, S. D. M. 1997, *ApJ*, 490, 493
- Noterdaeme, P., Petitjean, P., Ledoux, C., & Srianand, R. 2009, *A&A*, 505, 1087
- O’Meara, J. M., Prochaska, J. X., Worseck, G., Chen, H.-W., & Madau, P. 2013, *ApJ*, 765, 137
- Osterbrock, D. E. 1989, *Astrophysics of gaseous nebulae and active galactic nuclei*
- Ouchi, M., Shimasaku, K., Furusawa, H., Saito, T., Yoshida, M., Akiyama, M., Ono, Y., Yamada, T., Ota, K., Kashikawa, N., Iye, M., Kodama, T., Okamura, S., Simpson, C., & Yoshida, M. 2010, *ApJ*, 723, 869
- Park, J.-C., Kong, K., & Park, S. C. 2014, *Physics Letters B*, 733, 217
- Pawlik, A. H., Schaye, J., & van Scherpenzeel, E. 2009, *MNRAS*, 394, 1812
- Planck Collaboration, Ade, P. A. R., Aghanim, N., Arnaud, M., Ashdown, M., Aumont, J., Baccigalupi, C., Banday, A. J., Barreiro, R. B., Bartlett, J. G., & et al. 2015, *ArXiv e-prints*

Planck Collaboration, Aghanim, N., Ashdown, M., Aumont, J., Baccigalupi, C., Ballardini, M., Banday, A. J., Barreiro, R. B., Bartolo, N., Basak, S., Battye, R., Benabed, K., Bernard, J.-P., Bersanelli, M., Bielewicz, P., Bock, J. J., Bonaldi, A., Bonavera, L., Bond, J. R., Borrill, J., Bouchet, F. R., Boulanger, F., Bucher, M., Burigana, C., Butler, R. C., Calabrese, E., Cardoso, J.-F., Carron, J., Challinor, A., Chiang, H. C., Colombo, L. P. L., Combet, C., Comis, B., Coulais, A., Crill, B. P., Curto, A., Cuttaia, F., Davis, R. J., de Bernardis, P., de Rosa, A., de Zotti, G., Delabrouille, J., Delouis, J.-M., Di Valentino, E., Dickinson, C., Diego, J. M., Doré, O., Douspis, M., Ducout, A., Dupac, X., Efstathiou, G., Elsner, F., Enßlin, T. A., Eriksen, H. K., Falgarone, E., Fantaye, Y., Finelli, F., Forastieri, F., Frailis, M., Fraisse, A. A., Franceschi, E., Frolov, A., Galeotta, S., Galli, S., Ganga, K., Génova-Santos, R. T., Gerbino, M., Ghosh, T., González-Nuevo, J., Górski, K. M., Gratton, S., Gruppuso, A., Gudmundsson, J. E., Hansen, F. K., Helou, G., Henrot-Versillé, S., Herranz, D., Hivon, E., Huang, Z., Ilic, S., Jaffe, A. H., Jones, W. C., Keihänen, E., Keskitalo, R., Kisner, T. S., Knox, L., Krachmalnicoff, N., Kunz, M., Kurki-Suonio, H., Lagache, G., Lamarre, J.-M., Langer, M., Lasenby, A., Lattanzi, M., Lawrence, C. R., Le Jeune, M., Leahy, J. P., Levrier, F., Liguori, M., Lilje, P. B., López-Caniego, M., Ma, Y.-Z., Macías-Pérez, J. F., Maggio, G., Mangilli, A., Maris, M., Martin, P. G., Martínez-González, E., Matarrese, S., Mauri, N., McEwen, J. D., Meinhold, P. R., Melchiorri, A., Mennella, A., Migliaccio, M., Miville-Deschênes, M.-A., Molinari, D., Moneti, A., Montier, L., Morgante, G., Moss, A., Mottet, S., Naselsky, P., Natoli, P., Oxborrow, C. A., Pagano, L., Paoletti, D., Partridge, B., Patanchon, G., Patrizzii, L., Perdereau, O., Perotto, L., Pettorino, V., Piacentini, F., Plaszczynski, S., Polastri, L., Polenta, G., Puget, J.-L., Rachen, J. P., Racine, B., Reinecke, M., Remazeilles, M., Renzi, A., Rocha, G., Rossetti, M., Roudier, G., Rubiño-Martín, J. A., Ruiz-Granados, B., Salvati, L., Sandri, M., Savelainen, M., Scott, D., Sirri, G., Sunyaev, R., Suur-Uski, A.-S., Tauber, J. A., Tenti, M., Toffolatti, L., Tomasi, M., Tristram, M., Trombetti, T., Valiviita, J., Van Tent, F., Vibert, L., Vielva, P., Villa, F., Vittorio, N., Wandelt, B. D., Watson, R., Wehus, I. K., White, M., Zacchei, A., & Zonca, A. 2016, ArXiv e-prints

Prochaska, J. X., Worseck, G., & O’Meara, J. M. 2009, *ApJ*, 705, L113

Read, J. I., Wilkinson, M. I., Evans, N. W., Gilmore, G., & Kleyna, J. T. 2006, *MNRAS*, 367, 387

Ribaudo, J., Lehner, N., & Howk, J. C. 2011, *ApJ*, 736, 42

Ricotti, M., Pontzen, A., & Viel, M. 2007, *ApJ*, 663, L53

Robertson, B. E., Furlanetto, S. R., Schneider, E., Charlot, S., Ellis, R. S., Stark, D. P., McLure, R. J., Dunlop, J. S., Koekemoer, A., Schenker, M. A., Ouchi, M., Ono, Y., Curtis-Lake, E., Rogers, A. B., Bowler, R. A. A., & Cirasuolo, M. 2013, *ApJ*, 768, 71

Schenker, M. A., Ellis, R. S., Konidaris, N. P., & Stark, D. P. 2014, *ApJ*, 795, 20

Schneider, R., & Omukai, K. 2010, *MNRAS*, 402, 429

- Shapley, A. E., Steidel, C. C., Pettini, M., & Adelberger, K. L. 2003, *ApJ*, 588, 65
- Shibuya, T., Ouchi, M., Nakajima, K., Hashimoto, T., Ono, Y., Rauch, M., Gauthier, J.-R., Shimasaku, K., Goto, R., Mori, M., & Umemura, M. 2014, *ApJ*, 788, 74
- Shull, J. M., Harness, A., Trenti, M., & Smith, B. D. 2012, *ApJ*, 747, 100
- Sobral, D., Matthee, J., Darvish, B., Schaerer, D., Mobasher, B., Röttgering, H. J. A., Santos, S., & Hemmati, S. 2015, *ApJ*, 808, 139
- Sokasian, A., Abel, T., Hernquist, L., & Springel, V. 2003, *MNRAS*, 344, 607
- Songaila, A., & Cowie, L. L. 2010, *ArXiv e-prints*
- Stengler-Larrea, E. A., Boksenberg, A., Steidel, C. C., Sargent, W. L. W., Bahcall, J. N., Bergeron, J., Hartig, G. F., Jannuzi, B. T., Kirhakos, S., Savage, B. D., Schneider, D. P., Turnshek, D. A., & Weymann, R. J. 1995, *ApJ*, 444, 64
- Storrie-Lombardi, L. J., McMahon, R. G., Irwin, M. J., & Hazard, C. 1994, *ApJ*, 427, L13
- Tilvi, V., Papovich, C., Finkelstein, S. L., Long, J., Song, M., Dickinson, M., Ferguson, H. C., Koekemoer, A. M., Giavalisco, M., & Mobasher, B. 2014, *ApJ*, 794, 5
- Trac, H., Cen, R., & Mansfield, P. 2015, *ApJ*, 813, 54
- Treu, T., Schmidt, K. B., Trenti, M., Bradley, L. D., & Stiavelli, M. 2013, *ApJ*, 775, L29
- Tumlinson, J., Giroux, M. L., & Shull, J. M. 2001, *ApJ*, 550, L1
- Vanzella, E., Fontana, A., Pentericci, L., Castellano, M., Grazian, A., Giavalisco, M., Nonino, M., Cristiani, S., Zamorani, G., & Vignali, C. 2014, *A&A*, 569, A78
- Viel, M., Becker, G. D., Bolton, J. S., & Haehnelt, M. G. 2013, *Phys. Rev. D*, 88, 043502
- Viel, M., Lesgourgues, J., Haehnelt, M. G., Matarrese, S., & Riotto, A. 2005, *Phys. Rev. D*, 71, 063534
- Wechsler, R. H., Bullock, J. S., Primack, J. R., Kravtsov, A. V., & Dekel, A. 2002, *ApJ*, 568, 52
- Wilkins, S. M., Trentham, N., & Hopkins, A. M. 2008, *MNRAS*, 385, 687
- Worseck, G., Prochaska, J. X., McQuinn, M., Dall’Aglio, A., Fechner, C., Hennawi, J. F., Reimers, D., Richter, P., & Wisotzki, L. 2011, *ApJ*, 733, L24+
- Worseck, G., Prochaska, J. X., O’Meara, J. M., Becker, G. D., Ellison, S. L., Lopez, S., Meiksin, A., Ménard, B., Murphy, M. T., & Fumagalli, M. 2014, *MNRAS*, 445, 1745
- Zheng, Z., Cen, R., Trac, H., & Miralda-Escudé, J. 2010, *ApJ*, 716, 574